Carl von Ossietzky
Universität Oldenburg

und

Hochschule Emden - Leer

Studiengang

Engineering Physics

Masterarbeit

Titel

Quasi-phase matching for high-average power high harmonic generation

vorgelegt von

Hauke Onno Höppner

Betreuender Gutachter:

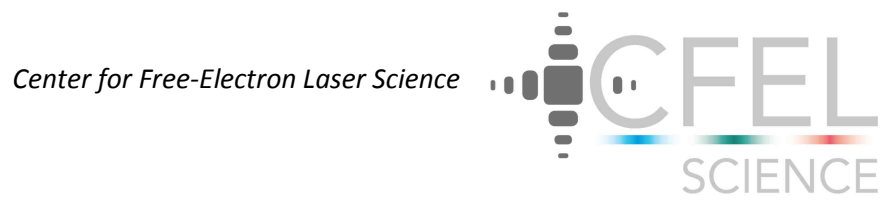**Prof. Dr. rer. nat. habil. Ulrich Teubner**

Zweitgutachter:

Prof. Dr. Adrian Cavalieri
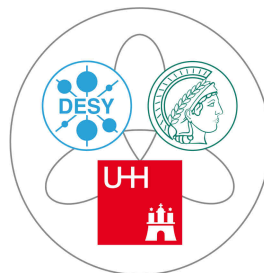
Oldenburg, 25.02.2013

Diese Arbeit wurde am

Center for Free-Electron Laser Science

in der Abteilung

Max Planck Research Department for
Structural Dynamics at the University
of Hamburg

Luruper Chaussee 149
22761 Hamburg
Germany

durchgeführt.

Abstract:

The currently running free-electron lasers (FELs) are primarily base on self-amplified spontaneous emission (SASE). Due to its stochastic process the X-ray pulse parameters change from shot to shot. There is a great scientific interest in improving the X-ray pulse parameters, such as the pulse shape and pulse spectrum, delivered by this ultra-intense and ultrashort source. One promising approach is to seed the FEL with high harmonics generated by an external XUV-source. At the „Freie-Elektronen Laser Hamburg II" (FLASH II) at the „Deutsche-Elektronensynchrotron" in Hamburg, it is planned to implement an external laser based XUV-seeding source. In order to generate the required seed energy of ~1 nJ in a variable spectral range from $10\,nm$ to $40\,nm$ (XUV - extreme ultraviolet) at $100\,kHz$ repetition rate, a new modular multi-nozzle XUV-source has been developed. The multi-nozzles create successive gas-jets in an open space geometry, enabling the nozzle to be used at high average power without a damage threshold. The multi-jet source enables high harmonic generation (HHG) in an inert gas by successive coherent superposition. In order to obtain coherent superposition, the phase between the fundamental laser frequency and the harmonics has to be adjusted between each single jet. The concept of quasi-phase-matching (QPM) is based on HHG-jets alternating with hydrogen jets, where the hydrogen acts as phase-matching medium to correct the phase acquired in the HHG-jet. Hydrogen is completely ionized at the used driver intensities $\geq 3 \cdot 10^{14}\,W/cm^2$ and therefore cannot contribute to the HHG-process. Atomic and plasma dispersion allow the control of the phase relationship between the fundamental and high harmonics by pressure tuning, in order to achieve coherent superposition of the generated harmonics in the multi-jet target. Proof of principle experiments exhibited significant enhancement for low average power driver lasers. In this thesis the macroscopic aspects for QPM are analyzed in a 1-d simulation. The results of the simulation provided the conditions for experimental tests of the dual-gas target at high repetition rates. The experimental part of this work has been accomplished at the „Institut für angewandte Physik" in Jena at a high power fiber amplifiers system with laser parameter: $400\,\mu J$ pulse energy, $580\,fs$ pulse duration (FWHM), and $75\,kHz$ repetition rate. For selected harmonics a maximal enhancement of the harmonic yield by a factor of 2 - 3 was achieved.

Kurzfassung:

Das wissenschaftliche Interesse an der Verbesserung der Pulsparameter von Freie-Elektronen Lasern (FEL) in Bezug auf Pulsform und Spektrum ist groß. Ein vielversprechender Ansatz ist das direkte "Seeden" des FEL's mit höheren Harmonischen durch eine externe XUV-Quelle. Für den Freie-Elektronen Laser Hamburg II (FLASH II) beim Deutsche-Elektronensynchrotron (DESY) in Hamburg ist eine derartige XUV-Quelle in der Planung vorgesehen. Um möglich effizient hohe Harmonische mit variablem Wellenlängenbereich von $10\,nm$ bis $40\,nm$ mit Wiederholrate von $100\,kHz$ zu erzeugen, wurde eine neue HHG-Quelle auf Basis eines modularen multi-Düsen Systems entwickelt. Die Düsen erzeugen sukzessive Gasstrahlen im offenen Raum im Vakuum. Die offene Geometrie ist notwendig, um die durch die hohen Wiederholraten entstehende hohe Durchschnittsleistung ohne Zerstörschwelle nutzen zu können. Die multi-Strahl-Quelle erlaubt die sukzessive Erzeugung von hohen Harmonischen in Edelgas, welche kohärent überlagert werden. Um die konstruktive Überlagerung zu gewährleisten, muss die Phasenbeziehung zwischen Fundamentaler und Harmonischen nach jedem Einzelstrahl angepasst werden (Quasi-Phasen-Anpassung). Dieses Verfahren der Quasi-Phasen-Anpassung wird mit einem dual Gas System realisiert. Zwischen die einzelnen HHG-Gasstrahlen wird jeweils ein Wasserstoff-Gasstrahl eingefügt. Im Wasserstoff lassen sich ab Intensitäten von $> 3{\cdot}10^{14}$ W/cm² wegen vollständiger Ionisation keine höheren Harmonischen mehr erzeugen. Durch die Plasma Dispersion lässt sich die Phasenbeziehung zwischen Fundamentaler und Harmonischen wiederherstellen und somit destruktive Interferenz vermeiden. Mit dieser multi-Strahl-Quelle lässt sich die harmonische Ausbeute nachweislich verbessern. Im Rahmen der Masterthesis wurde neben einer eindimensionalen Simulation, die multi-Strahl-Quelle erstmalig bei hohen Wiederholraten getestet. Der experimentelle Teil der Arbeit wurde am Institut für angewandte Physik (IAP) in Jena an einem Hochleistungs-Faserverstärker bei $400\,\mu J$ Pulsenergie, $580\,fs$ Pulsdauer (FWHM) bei einer Pulswiederholrate von $75\,kHz$ getestet. Es konnte für vereinzelte Harmonische eine maximale Verbesserung der Photonenausbeute um den Faktor 2-3 erzielt werden.

Table of Contents

1 Introduction

High harmonic generation (HHG) is a phenomenon of high intensity laser physics to convert driver pulses, which can span from far-infrared to the visible spectrum, into coherent extreme ultraviolet (XUV) radiation. The process was first discovered by A. McPherson in 1987 [1] in rare earth gases. In 1989 X.F. Li [2] reported the first multiple harmonics of a driver laser. Next to gas targets, high harmonics can also be generated by laser-produced plasmas of solid targets [3]. Since then a considerable effort has been devoted not only to the theoretical understanding of the nonlinear HHG-process [4,5], but also to the research of coherent laser-based tabletop XUV-sources.

Despite the existence of an accepted approach of a quantum mechanical description of the HHG-process [5], it is not possible to find best conditions by systematic studies due to the computational complexity of the problem [6]. For this reason the focus of current experimental research concentrates on determining the best driver lasers, media and additional techniques to allow the most efficient HHG.

In general HHG-based XUV-sources suffer a low photon flux, because of relatively low conversion efficiency of the HHG-process in gases. Typical values for the conversion efficiency are 10^{-6} in the range of $100\ eV$, and 10^{-15} in the range of keV [7]. The driver intensity for efficient gas harmonics generation is limited to a range between 10^{14}-10^{16} W/cm^2, because a complete ionization disrupts the HHG-process. On the contrary, the conversion efficiency of solid target plasma harmonics scale with no limitation to applied laser intensity [3]. However, for high repetition rate applications at 100 kHz solid target harmonic generation is inefficient, because intensities between 10^{17}-10^{19} W/cm^2 are not approachable with state of the art laser systems.

In addition to self-absorption, HHG is limited by the phase matching conditions and is a result of different phase velocities of the driving and the harmonic field generating a phase-mismatch. This directly affects the interaction length and limits the ideal quadratic scaling of the HHG-process, because a longer interaction length can cause destructive interference. Matching the different phase velocities (phase matching) becomes necessary in order to maximize the harmonic yield.

Classical phase matching techniques have certain limits with regard to enhancement of the harmonic yield and the extension of the cut-off energy or corresponding wavelength. While the cut-off scales monotonically with the intensity, the phase matching ability drops at high order harmonics. The critical ionization level, depending both on the driver intensity and the gas medium, limits true phase matching at higher intensities [8].

In order to overcome this limitation the quasi-phase matching (QPM) technique is a possible approach. It provides the possibility to enhance the harmonic yield by avoiding the classical phase matching limit and follows the idea of coherent superposition of harmonics generated in successive sources. The HHG-process has to be suppressed at positions where the driver field is out of phase with the high harmonics. Thus, destructive interference will be prevented. Upon optimal conditions this leads to coherent superposition of high harmonics in multiple in-phase areas and the harmonic yield can grow with the propagation monotonically. Thus the effective interaction length can be longer than in the case of classical phase matching. The ideal QPM-signal grows quadratically with the number of in-phase areas (N_{QPM}^2) [8] and is mainly limited by self-absorption and critical ionization.

For several applications not only the harmonic yield and the cut-off energy are the essential factors, but the spatial and temporal coherence properties of the generated harmonics and their control are also important. In order to generate customized and controlled attosecond pulses, the spatial and temporal coherence properties have to be controlled [9].

In the past decade, several different QPM techniques have been reported, which either modulate the intensity, such as counter propagating pulses [10], multimode beating [11], modulated waveguides [12]; or modulate plasmas structure (composite) [13]. Another approach is to modulate the gas density directly [14]. In general, all these approaches showed the validity of the QPM principle for HHG, but improvements can be carried out with respect to the N_{QPM}^2 dependence for scaling the harmonic yield and coherence control ability [14]. Furthermore, approaches that use free space geometry, such as the modulated gas density, have no damage threshold. Thus free space geometry becomes interesting for HHG with high average power laser systems at multi-kHz repetitions rate.

The simplest version of the density modulation technique in the free space geometry is to use several gas targets, which are separated in space (vacuum) to match the relative phase [14,15]. However, in this approach, the target design cannot be compact. The effect of the vacuum phase-shift is too weak and has to be compensated with large separation distances to realize QPM. The separation distance becomes relatively large, compared to the Rayleigh length of a focused driver pulse of a realistic laser amplifier. Considering that each jet of target must be inside the Rayleigh length, only a few QPM periods can be realized, which limits the maximal enhancement factor.

To realize higher target densities, the spacing between the single gas jets has to be reduced. Therefore a medium has to be inserted, which introduces the phase-shift in a more efficient way. It should be adjustable and remains passive with respect to harmonic generation at the same time. Fully ionized hydrogen fulfills those requirements as a passive gas [16]. This makes it feasible to de-

velop a compact dual-gas target with alternating jets. With this target the ability to adjust the pressure of the HHG and phase matching gases separately result in an improvement of the harmonic yield and the ability of efficient coherence control [17].

The development of the dual-gas target is a sub-project of the "Freie-Elektronen Laser Hamburg 2" (FLASH 2) at the research facility "Deutsches Elektron Synchrotron" (DESY) in Hamburg. FLASH 2 is designed to be seeded by an external HHG XUV-source next to the classical SASE-mode (self-amplification by spontaneous emission) [18]. Compared to the SASE-mode, where the amplification evolves from spontaneous emission, the external seeding transfers the spectral and temporal properties of the HHG-pulse to the FEL pulse. As a result shorter pulses with a smoother temporal profile are expected and the energy spectrum becomes more stable [16]. To seed a FEL the seed energy has to exceed approximately $> 1\,nJ$ in the undulator [16]. At intra-burst repetitions rates up to $100\,kHz$, this is a challenge because a new kind of driver laser type, efficient HHG and low-loss beam transport are needed. The prototype development of the HHG driver laser is in an advanced stage and can imitate the burst-mode pulse structure of FLASH 2 [19], [20]. To improve the HHG-efficiency at requested repetitions rates, it is the long term goal to use the QPM technique in order to achieve sufficient photon flux to obtain seeding capability in the spectral range between $10\,nm$ to $40\,nm$.

Additionally, the high repetition rate XUV-source is of great interest for research in photoemission spectroscopy. The free gas jet geometry of the dual gas HHG-target appears to be a promising approach for the upcoming generation of high average power lasers at high repetitions rates. In addition the phase matching capabilities, the dual-gas target is able to operate at high-average power and high thermal loads.

In this thesis the macroscopic aspects for QPM have been analyzed in a 1-d simulation. The results of the simulation provide the starting conditions for experimental tests of the dual-gas target, which has been developed within the FLASH II project [16]. The target has been investigated experimentally at multi-kHz repetitions rate and at high-average powers for the first time. The experiment was carried out with a driver laser system based on fiber chirped-pulse amplification (FCPA) at the "Institut für angewandte Physik" (IAP) Jena [21]. At the IAP high order harmonic generation was performed at $75\,kHz$ with $400\,\mu J$ pulse energy and $480\,fs$ pulse duration (FWHM) at a center wavelength of $1030\,nm$. The central problem was the implementation of QPM at the given laser parameters. Examined here were the aspects of the target performance with respect to the signal gain of the harmonic yield as well as the cut-off extension. For successful seeding, other parameters are important such as: the beam quality, time structure, and both spatial and temporal coherence. However, those parameters are not in the scope of this work. Past experiments

with the dual gas target has been successfully accomplished at $800\,nm$ center wavelength with pulse durations at $3.5\,fs$ and $25\,fs$ at a few kHz repetitions rate range [22]. Much higher peak intensities are achievable and permit long focal length geometries.

2 Theoretical Background

2.1 High Harmonic Generation: a first overview

High harmonic generation occurs when a short, intense laser field interacts with an atomic or molecular gas. By focusing an intense femtosecond pulse (in the range of 10^{14}-10^{16} W/cm^2) into a target e.g. inert gas, a nonlinear process develops and several higher order harmonics q are emitted in forward direction – see Figure 1. A characteristic spectrum is shown in Figure 2. A HHG emission spectrum has a characteristic distribution, which can be divided in: (i) perturbative regime, (ii) plateau harmonics, (iii) cut-off.

The Perturbation theory can be used to describe the generation of lower order harmonics. They are produced at low intensities present during the rise and fall of spatial and temporal wings of the intensity profile of a laser pulse. The decrease of the harmonic yield follows a usual q-power of the nonlinear susceptibility ($\chi^{(q)}$) [23]. Characteristic feature is the decreasing signal of single-atom response with increasing q at low harmonic order regime ($q \leq 7 - 9$).

The amplitude of the harmonics in the plateau region is relatively constant with increasing harmonic order. These higher order harmonics are generated at higher laser intensities. Here, perturbation theory becomes invalid as the laser field approaches the inner-atomic field strength.

The plateau regime is followed by cut-off behavior, where the amplitudes of the harmonics show a strong amplitude drop.

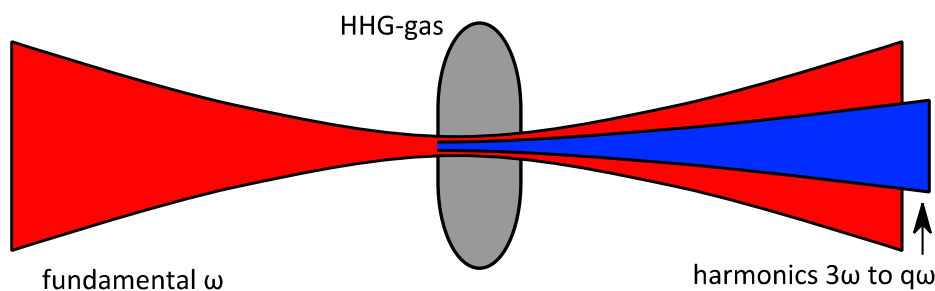

HHG-gas

fundamental ω

harmonics 3ω to qω

Figure 1: Schematic overview of the HHG interaction zone in a free jet geometry. An intense laser pulse focused into a noble gas jet induces the nonlinear HHG-process.
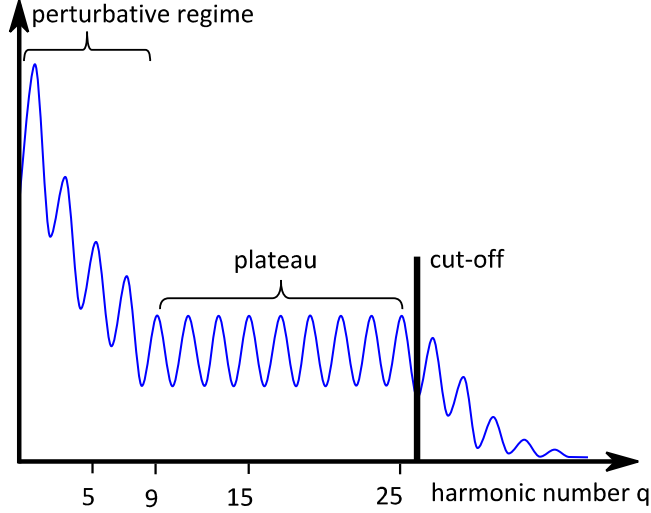
Figure 2: Schematic harmonic spectrum: The spectrum can be divided into three regimes: perturbative, plateau and cut-off. The cut-off is determined by the maximum kinetic energy of the electron. HHG in noble gas generates only odd harmonics.

The maximal microscopic photon energy is usually referred to cut-off energy or wavelength. The cut-off law, which can be obtained using classical [4] or quantum mechanical [5] approaches, allows to calculate the cut-off energy

$$\hbar \varpi_{max} = q_{max} \hbar \varpi = 3.17 \cdot U_p + I_p, \tag{2.1}$$

where q_{max} is the maximal harmonic number, ω fundamental frequency, ω_{max} cut-off frequency, I_p the ionization potential of the atom and the pondermotive potential. U_p is the time averaged kinetic energy of the electron and given by:

$$U_p = \frac{e^2 E_0^2}{4 m_e \omega^2} = 9.33 \cdot 10^{-14} \cdot I \left[\frac{w}{cm^2} \right] \cdot (\lambda[\mu m])^2 eV, \tag{2.2}$$

where E_0 is the laser field amplitude, e - the electron charge, m_e - the electron rest mass, I - the laser intensity and λ - the driver laser wavelength. The cut-off law describes the characteristic behavior of the HHG concerning the highest resulting photon energy. The maximal photon energy is monotonically increasing with binding energy or pondermotive potential U_p. The pondermotive potential itself scales with the driver pulse intensity and the wavelength. However, due to the macroscopic effects, which are defined by the gas properties, driver intensity and wavelength, the scaling of the cut-off law is limited and can have tremendous influence on the harmonic yield.

The scaling of the harmonic yield is a combination of microscopic and macroscopic effects. The microscopic process of HHG is described on atom level by the single atom response. The atomic properties are an important parameter for the scaling. Considering the aspects of the cut-off extension, helium is well suited because of the high binding energy. However, the resulting harmonic yield would be low, because of the small effective nonlinear susceptibility of

helium. Next to the atom properties, the single atom response is related to the driver wavelengthλ. The driver wavelength has strong influence on the scaling. In the plateau region the harmonic intensity scales with λ^{-5} and at the cut-off with λ^{-6} [6]. Although the cut-off can be extended by using longer driver wavelength, the generation of higher harmonics (cut-off range) becomes inefficient. The amplitude single atom response decreases at higher wavelength and an efficient conversion becomes difficult [6].

Macroscopically the harmonic yield is composed of the sum of the electro-optical fields of all the participating atoms N. As long as the electro optical field of each emitter can superpose coherently, the harmonic yield scales with N^2 at ideal conditions. However, due to macroscopic propagation effects coherent superposition becomes limited. Phase matching techniques have to be applied in order to lock the phase of contributing emitters to avoid destructive interference and achieve the N^2 scaling.

2.2 Single atom response

Different models have been developed to describe the activity of individual atoms contribution to the HHG-process. The most successful one is the so called three-step model (TSM), a semi classical approach introduced by P. Corkum [4]. In this model the atomic potential becomes strongly distorted by the optical laser field and tunnel ionization is favored (Figure 3).

With rising slope of a strong laser field the atomic potential is bent and decreases the barrier. The electron can escape with a not-zero probability to the continuum by tunnel ionization (1). After the field reverses the sign, the electron is accelerated back to the parent ion and gains kinetic energy (2). The accelerated electron can recombine with a relatively small probability (3).
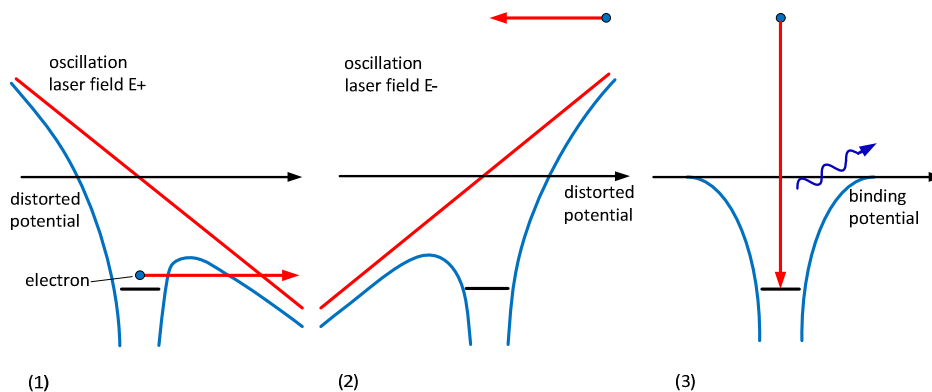
Figure 3: Schematic overview of the single-atom response in the three step model. (1) A strong laser field bents the atomic potential and decreases the barrier. The electron can tunnel through the barrier with a certain probability. (2) The electron is accelerated to the parent ion and gains kinetic energy. (3) The electron can recombine with a non-zero probability with the parent ion and generates a photon with increased by the energy which is gained by the acceleration.

In case of recombination a relaxation occurs and a photon with energy

$$E_{HHG} = I_P + E_{kin} \qquad (2.3)$$

will be emitted.

The reason why the harmonic spectrum shows a comb structure (Figure 2) can be led back to periodically generation of harmonics in time, due to the oscillations of the electric field. The oscillating driving field creates a pulse train of harmonics in the time domain, where each single pulse has duration shorter than the half cycle of the driving field. The resulting pulses can be in the attosecond regime and is referred as attosecond pulse train in the literature [24] – see Figure 4. The coherent addition of the emission from each half-cycle leads to a periodicity in the HHG emission in time. The result is the characteristic frequency comb with a 2ω spacing in the frequency domain.

Only odd harmonics are generated in atomic gases, due to the inversion symmetry of the interaction [25]. No difference can be observed when the electron tunnels through the barrier when the electric field is -E or +E and the binding potential is symmetric. All three steps of the model are described separated in the next subsections. A particular focus is on the ionization process and its quantification, because the resulting ionization rate represents the base for the simulation.
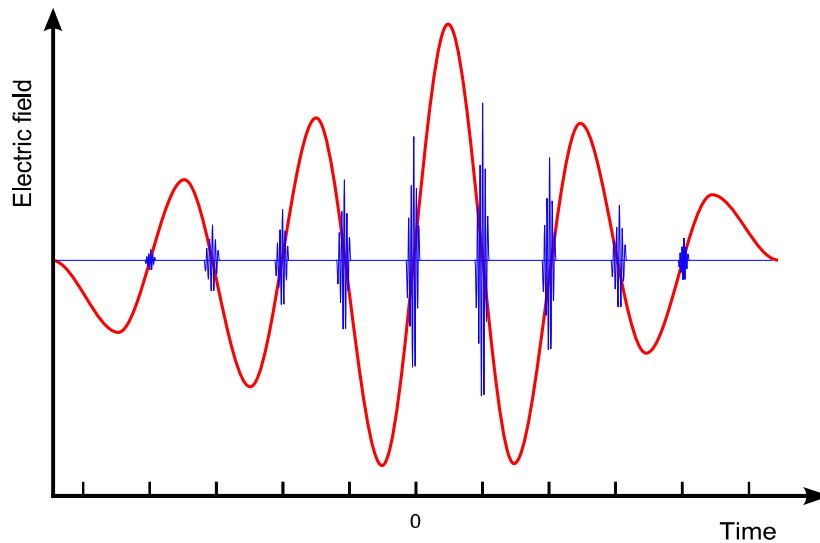

Figure 4: Temporal development of the attosecond pulse train (blue) and the electrical field of the laser pulse (red). The harmonic pulses are created twice per driver laser cycle. This behavior leads to the characteristic with half cycle spacing or comb structure with a 2ω spacing in the frequency domain.

2.2.1 Ionization

In the first step of the TSM an –optical field ionization- occurs. This can be either multiphoton ionization (MPI) or tunnel ionization (TI). In MPI process the potential wall is being bridged by the summation of several driver photons (see Figure 5). To observe MPI the intensity must be large enough. The MPI is described by the perturbative theory, but it is only valid for laser fields lower than the binding potential. If the laser field becomes comparable strong as the atomic binding potential, the perturbative theory is not valid anymore. At these intensities the potential barrier will be distorted drastically.

The length of the barrier will be reduced and the electron can tunnel with a higher probability. To discriminate the dominating process, since MPI and TI are no simultaneous effects, Keldysh formulated a criterion to define the dimensionless Keldysh parameter [26]

$$\gamma = \sqrt{\frac{I_p}{2U_p}}.$$ (2.4)

It compares basically binding energy and pondermotive energy. Multiphoton ionization prevails in the regime $\gg 1$. The tunnel effect becomes the dominating process at $\gamma \leq 0.5$, which emerges in the infrared spectral regime in intensities range between 10^{14} to $10^{16} W/cm^2$ [8]. Tunnel ionization can be considered as the dominating ionization process for high order HHG.

The first description of the tunnel ionization process was provided by the Perelomov Popov and Terentev (PPT)-theory [27], which was only valid for hydrogen. The Ammosov-Delone-Krainov (ADK)-theory [28], an extension of the PPT-theory, considers more complex systems.
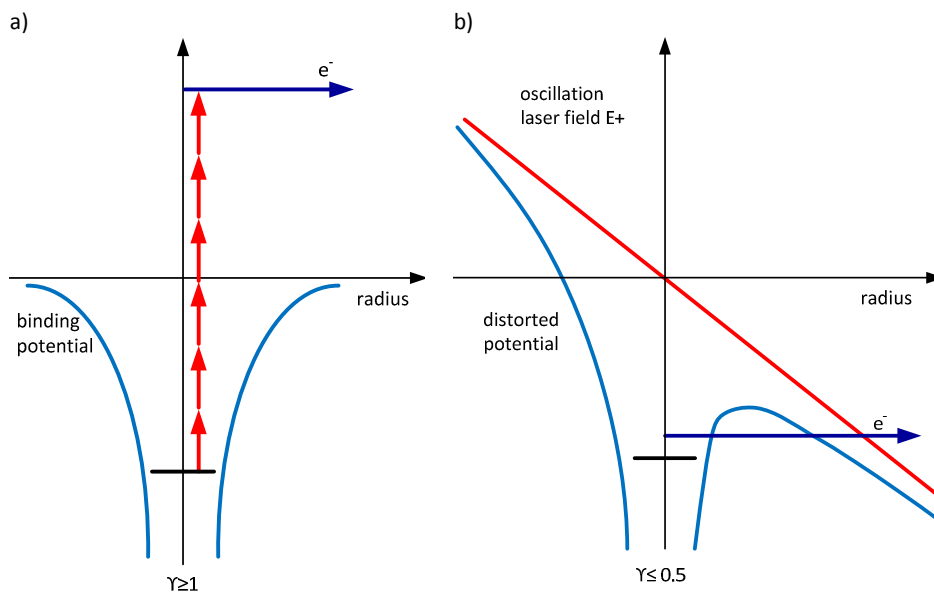

Figure 5: Comparison of the of a) multiphoton ionization and b) tunnel ionization process.

Ionization rates of arbitrary atoms can be calculated. It is important to mention that the ADK-theory treats only one electron by time. The atom is considered to be in the ground state, before a new ionization sequence can occur.

The analytical calculation of instantaneous ionization rates are given by averaging the rate in a constant field over one laser period. This approximation is known as low-frequency or quasi static approximation and is valid for electric field oscillations much slower than the tunneling time.

The tunnel rate for optical tunnel ionization w for the binding energy E, with orbital quantum number l and magnetic spin m is given by [28]

$$w(t) = E \cdot f(l,m) \cdot |C_{n^*,l^*}|^2 \cdot \left(\frac{3E_0}{\pi F}\right)^{1/2} \left(\frac{2F}{E_0}\right)^{2n^*-|m|-1} \cdot exp\left(-\frac{2F}{3E_0}\right) \qquad (2.5)$$

where the field amplitude of the laser pulse is E_0 and $F = (2E)^{3/2}$. The atom is considered as a hydrogen-like state with just one outer shell electron. Taking into account the shield effect of the inner electrons the effective quantum states n^* and l^* become introduced. They are defined as

$$n^* = Z(2E)^{-1/2}, \qquad (2.6)$$

where Z is the charge number of the ion and

$$l^* = n^* - 1. \qquad (2.7)$$

The coefficients $f(l,m)$ and $|C_{n^*,l^*}|^2$ are given by

$$f(l,m) = \frac{(2l+1)(l+|m|)!}{2^{|m|}(|m|)!\,(l-|m|)!}, \qquad (2.8)$$

$$|C_{n^*,l^*}|^2 = \frac{2^{2n^*}}{n^*\Gamma(n^*+l^*+1)\Gamma(n^*l^*)}. \qquad (2.9)$$

To obtain the total time dependent ionization rate, the contribution of all m-states has to be considered, which is given by

$$w_{ADK}(t) = \frac{\left(\sum_{i=0}^m w_i(t)\right)}{2l+1}. \qquad (2.10)$$

Solving this rate equation leads to the free electron density. The free electron density/fraction is defined as [29]

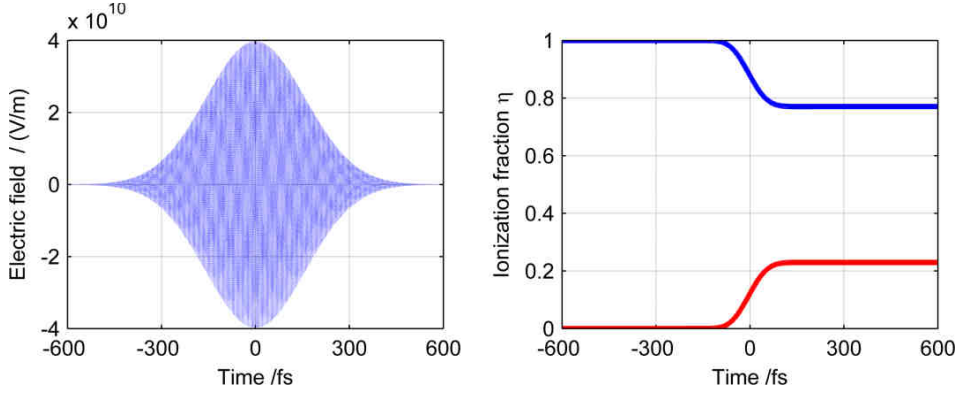$$\eta(t) = n_0\left(1 - exp\left(-\int_{-\infty}^t w_{ADK}(t')dt'\right)\right), \qquad (2.11)$$

Figure 6: (left) Calculated electric field for a 480 fs (FWHM) Gaussian laser pulse with a peak intensity of $2 \cdot 10^{14} W/cm^2$ at 1030 nm center wavelength. (right) Calculated resulting relative fraction for natural atoms (blue) and free electrons (red) in argon for the pulse given in (a).

where n_0 it the neutral atom density. In Figure 6 the evolution of the ionization fraction of neutral atoms and single ions in argon for a given pulse are shown. The ionization fraction η is an important parameter for the phase matching process. The connection is explained in detail in subsection (2.3.1).

2.2.2 Acceleration

After the electron is delocalized from the parent ion by tunnel ionization, it can interact with the still present electric field. The field reverses the sign and accelerates the electron back to its mother ion.

The interaction of the electron and the electric field can be described with a classical concept to obtain the time dependent kinetic energy and path of the electron. The resulting force on the electron in an electric field is defined as

$$F(t) = m \cdot \ddot{z}(t) = e \cdot E(t), \tag{2.12}$$

where m and e are the electron mass and charge respectively, and $\ddot{z}(t)$ the acceleration. The linear polarized electric field is given as,

$$E(t) = E_0 \cos(\omega_0 t), \tag{2.13}$$

E_0 and ω_0 denotes the field amplitude and frequency, respectively. The acceleration $\ddot{z}(t)$ of the electron can be derived by transposing Eq. (2.12)

$$\ddot{z}(t) = \frac{eE(t)}{m} = \frac{d\dot{z}(t)}{dt} \tag{2.14}$$

The electron is ejected at t=t$_I$. The velocity of the electron $\dot{z}(t)$ can be obtained by solving Eq. (2.14) by integration with the initial conditions

$$\dot{z}(t_I) = 0. \tag{2.15}$$

The resulting velocity is given by

$$\dot{z}(t) = \int_{t_I}^{t} \frac{eE(t)}{m} dt = \frac{eE_0}{\omega m}(\sin(\omega t) - \sin(\omega t_I)). \qquad (2.16)$$

Via this expression the electron path or trajectory can be derived by integrating the velocity with the initial condition

$$z(t_I) = 0, \qquad (2.17)$$

which results in:

$$z(t) = \frac{eE_0}{\omega m}\left(\omega(t - t_I)\sin(\omega t_I) - \cos(\omega t) + \cos(\omega t_I)\right). \qquad (2.18)$$

To deduce an expression for the kinetic energy the electron velocity and trajectories can be used. It is helpful to introduce the recombination time t_R, which can be evaluated numerically by taking into account the boundary condition that the electron needs to recombine with parent ion at $z(t_R) = 0$. On closer examination the trajectories in one optical cycle can be distinguished into so called short and long trajectories.

The electrons with a long trajectory are created directly after the peak of the electric field between 0 and $0.05\,T$, where T is the length of one optical cycle. They can recombine between 0.7 and $1\,T$. The electrons with a short trajectory are created between 0.05 and $0.25\,T$ and recombine between 0.25 and $0.7\,T$ – see Figure 7. Other trajectories cannot lead to a recombination.

A fundamental requirement for the HHG-process is linear polarized light. In case of elliptical or circular polarized light the trajectory cannot end in the initial position ever $z = 0$ and a recombination is not possible [4].
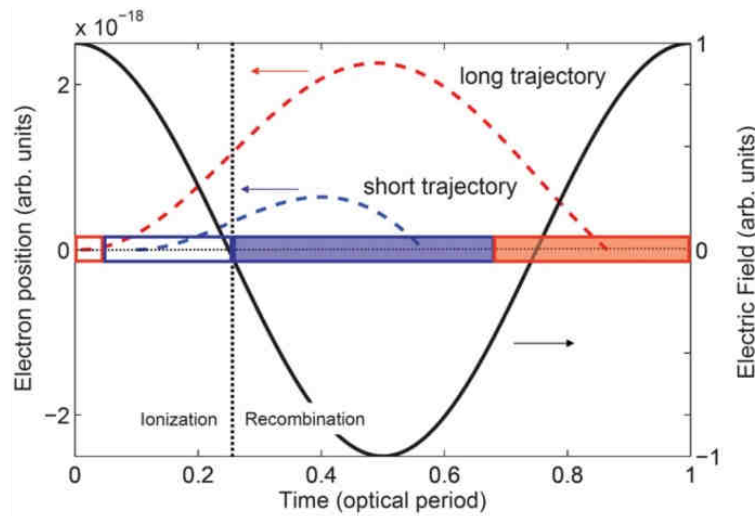

Figure 7: Concept of two electron trajectories in HHG. Ionization and recombination times for the long (red area) and short (blue area) trajectory in a driving laser field (black solid). Two example trajectories are implemented for a short trajectory (dashed blue) ionized at $T = 0.1$

With t_R the return velocity $\dot{z}(t_R)$ can be determined by Eq. (2.16) and leads to the resulting kinetic energy

$$E_{kin} = \frac{1}{2}m\dot{z}(t_R)^2 = \frac{1}{2}\frac{e^2 E_0^{\,2}}{\omega^2 m^2}(\sin(\omega t_R) - \sin(\omega t_I))^2, \qquad (2.19)$$

which can be transformed by an expression with U_P :

$$E_{kin} = 2 \cdot U_p(\sin(\omega t_R) - \sin(\omega t_I))^2. \qquad (2.20)$$

Depending on the "birth time" of the electron within the optical cycle of the driver pulse it can be either departed from the parent ion and a recombination will be impossible, or it participates in the HHG-process. It is to mention that recombination is only one effect which can occur. Other effects like electron-electron interactions and sequential ionization can occur also.

2.2.3 Recombination

In the third step of the TSM the before separated and accelerated electron can recombine with the parent ion. The recombination leads to a relaxation into the ground state. This transition causes the emission of a photon with the energy

$$E_{HHG} = I_P + E_{kin}. \qquad (2.21)$$

The recombination happens with a certain probability, because not all ionized electrons participate in the recombination process. Only electrons which fulfill the condition for a trajectory resulting in $z(t_R) = 0$, can contribute. The maximal kinetic energy

$$E_{kin,max} = 3.17 \cdot U_P, \qquad (2.22)$$

can only be obtained by electrons, which ionize at $0.05\,T$ and recombine at $0.7\,T$ of the optical pulse –see Figure 7. This so called cut-off trajectory and defines the cut-off energy:

$$\hbar\omega_{max} = q_{max}\hbar\omega = 3.17 U_p + I_p. \qquad (2.23)$$

Different trajectories, than the cut-off trajectory, result in lower photon energies, which contribute in the plateau regime of the spectrum. Furthermore, each trajectory is generated at different times within a half cycle of the optical pulse – cf. Figure 7. The superposition of high-order harmonics may lead to attosecond pulses in the time domain [24]. The fact of different timings of the trajectories, leads to an energy chirp in the intra cycle harmonic attosecond

pulse [30]. The contributions of the short trajectories have a positive chirp and the long trajectory contributions a negative one, which is referred as atto-chirp. In the single atom response both contributions are weighted equally. To compress a chirped pulse towards the fourier-limit via a chirped multilayer mirror, only short trajectories with the positive chirp should be present [17,31]. A chirped mirror is composed of dielectric multilayer films. Thereby the film structure varies in the thickness, so that the harmonics at different wavelength are reflected at different depths in the layer structure. The introduced wavelength dependent delay corrects the phase relation of the harmonics. However, the fabrication of adequate chirped multilayer mirrors is difficult in the XUV spectrum, because of the thin layer structure. To avoid chirped multilayer mirrors another method can be applied. Via adequate filtering the low order harmonics can be separated from the cut-off harmonics. The cut-off harmonics are generated in phase and are consequently unchirped. The methods for fourier-limited attosecond pulse generation will not be discussed in detail in this work.

2.3 Propagations effects

2.3.1 Phase matching

The three step model describes the single atom response in the HHG-process. The macroscopic response is not defined by one atom, but the superposition of all individual harmonic fields of an extended gas ensemble. In the ideal case the individual fields coherently superpose. However, propagations effects have to be considered for a complete description of the macroscopic HHG-process. Harmonic radiation is emitted as soon as the driver pulse enters the gas jet at $z_1 = 0$. The propagation of a one dimensional plane wave in z direction follows the equation

$$A(z,t) = A_0 \cdot \cos(\omega \cdot t + \vec{k} \cdot z) = A_0 \cdot \cos(\varphi), \qquad (2.24)$$

where A_0 is the maximal Amplitude, ω the optical angular frequency, $\vec{k}$ the wave vector and φ the phase. The wave number $k = |\vec{k}|$ describes the phase delay per unit length during propagation and is a function of the wavelength λ

$$k(\lambda) = n(\lambda) \frac{\omega}{c_0}, \qquad (2.25)$$

where n is the wavelength related complex refractive index and c_0 the speed of light in vacuum. The initial phase of the harmonics is coupled to the electric field of the driver laser. However, driver field and generated harmonics propagate after the generation with different phase velocities v_{ph} in the gas target, which is defined as

$$v_{ph} = \frac{\omega}{k(\lambda)}. \qquad (2.26)$$
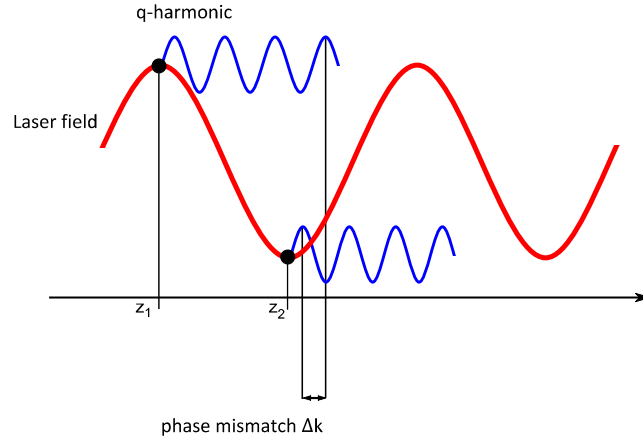
Figure 8: Schematic of the phase-mismatch Δk developing of two harmonics generated in different location in space due to different phase velocities of laser field and harmonics.

As a consequence a phase-mismatch $\Delta k = |k_{Laser} - k_q|$ occurs between harmonics generated at z_1 and $z_2 > z_1$, which is shown in Figure 8. The harmonic yield can grow monotonically by superposition of the individual fields till the phase-mismatch $\Delta k = \pi$, which corresponds to the coherence length

$$l_c = \frac{\pi}{|\Delta k|}.$$
(2.27)

A longer interaction length causes oscillations of the harmonic yield, due to alternating constructive and destructive interference, with the period of $2 \cdot l_c$ as shown in Figure 9. The maximal harmonic yield is limited by these oscillations. To maximize the efficiency of the HHG-process the phase difference between harmonics and driver field has to be minimized. This process is called phase matching and the absolute phase-mismatch Δk between driver laser and created harmonic of the qth order must satisfy the phase matching condition,

$$|\Delta k| = |k_q - q \cdot k_{Laser}| = 0.$$
(2.28)

The wave vector of the driver laser and harmonics is k_{Laser} and k_q respectively. Perfect phase matching is achieved at $|\Delta k| = 0$ and would lead to an exponential growth. This cannot be realized under experimental conditions, because of the wavelength dependency of $|\Delta k|$ and the spectral width of driver field and harmonics. The behavior of perfect und imperfect phase matching is shown in Figure 9.

In order to match the phases, it is important to know the propagation characteristics. The wave vector k for an optical electromagnetic wave passing through a gas/plasma has several contributions, which have to be accumulated. For the given free space jet HHG setup, k is given by [32],

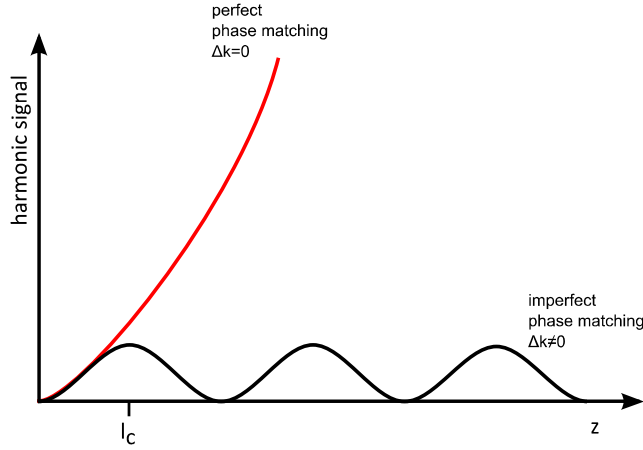$$k(\lambda) = k_{vac}(\lambda) + k_n(\lambda) + k_p(\lambda) + k_{geo}(\lambda),$$
(2.29)

Figure 9: Qualitative effect on the harmonic signal due to phase-mismatch. Occurring phase-mismatch limits the N² scaling relation and the harmonic signal is oscillating with the propagation in the HHG medium. By applying a phase matching technique the phase-mismatch can be reduced and the effective HHG length can be improved, which is defined by the coherence length l_c and correspondence to a phase-mismatch of π.

where k_{vac} describes the propagation through vacuum. The phase shift term k_{geo} is induced by the geometrical phase shift or Gouy-shift, which is related the focus geometry. The Gouy-shift is an additional acquired phase shift of π, occurring in the propagation of focused Gaussian beams, going from the far field to the far field behind the focus [33]. The Gouy-shift directly affects the phase relation between driver field and harmonics and limits the phase matching ability. The contribution of k_{geo} is always negative and is given by

$$k_{geo} = -arctan\left(\frac{z}{z_R}\right), \qquad (2.30)$$

where z_R is the Rayleigh length of the focused laser beam, which is defined by the focus geometry. To minimize the influence of the geometrical phase shift it is recommended to choose the target length $l_{target} \ll z_R$.becomes $k_{geo} \approx 1/z_R$.

The other two terms k_n and k_p describe the propagation through neutral gas and plasma respectively. Both terms depend mainly on the gas pressure, gas type and the laser intensity dependent tunnel ionization rate. The neutral gas dispersion is given by

$$k_n \approx \frac{2\pi}{\lambda} \cdot N_n \cdot n(\lambda), \qquad (2.31)$$

where n is the wavelength dependent atomic refractive index at a gas density corresponding $1\ atm$ and N_n the density of neutral atoms. N_n is related to the gas pressure p and the tunnel ionization fraction η given by Eq.(2.11). The neutral gas dispersion contributes positively to the phase vector mismatch Δk. The plasma dispersion is induced by free oscillating electrons and defined as

$$k_p \approx -N_e \cdot r_e \cdot \lambda, \tag{2.32}$$

where $r_e = 2.818\,fm$ is the classical electron radius and N_e is the free electron density. N_e depends on the pressure p , the tunnel ionization fraction η and the density of the gas atoms at atmospheric pressure. The plasma dispersion contributes negative to phase vector mismatch Δk .

Using the Eq.(2.30-2.32) a total expression for $|\Delta k|$ can be derived [16].

$$\begin{aligned} |\Delta k| \approx \frac{2\pi}{\lambda} \cdot q \cdot (1 - \eta) \cdot p \cdot \Delta n - \\ -p \cdot N \cdot \eta \cdot r_e \cdot \lambda \cdot \left(q - \frac{1}{q} \right) - \\ -(q - 1) \cdot arctan \left(\frac{z}{z_R} \right), \end{aligned} \tag{2.33}$$

where N is the atom density at $1\,atm$. Δn is introduced to describe the difference between the corresponding refractive index of the driver laser and the harmonic at $1\,atm$. It is given by

$$\Delta n = n_{Laser} - n_{q.} \tag{2.34}$$

As defined in Eq. (2.33) multiple parameters can be adjusted for phase matching. The atomic and plasma density have a major influence on the phase shift, which depends linear on the pressure. By changing the pressure the influence on Δk by atomic and plasma dispersions is in the opposite direction. Since tunnel ionization fraction η and atomic fraction $(1 - \eta)$ are directly coupled, the influence on Δk_n and Δk_p changes with different slopes. Both effects together allow phase matching. A pressure curve is shown in Figure 10 for different intensities.

It can be observed as well, that the intensity affects the slope, because η is a function of intensity – see Eq.(2.11). Therefore the intensity is the second important tuning parameter for phase matching. However, changes in the intensity lead to different cut-off conditions as well Eq.(2.1). It is a feasible method to move the focus plane before the gas jet, because the beam diverges after the focus and leads with the further propagation to a decreased intensity. At the same time the Gouy-shift induced phase shift changes with reversed sign. The interactions of both effects allow phase matching.

In case of a single jet geometry the influence of the harmonic intensity by dephasing can be expressed as [14]

$$I_q \propto N_a^2 \cdot \frac{sin \left(\frac{l_{med} \cdot \Delta k}{2} \right)^2}{\Delta k^2}, \tag{2.35}$$

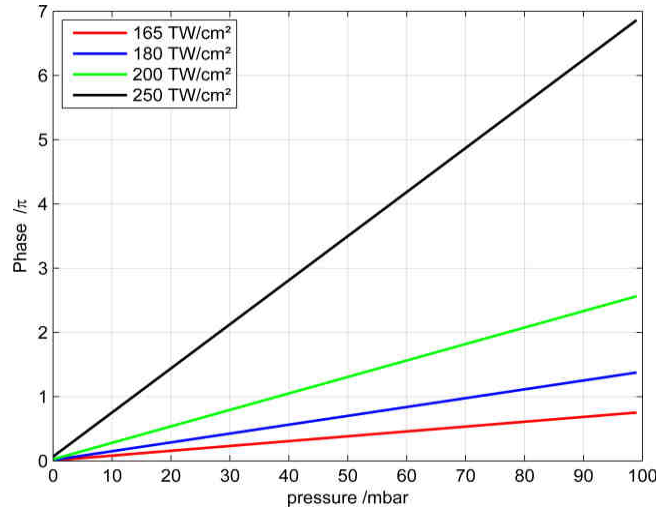where N_a is the number of participating radiators created by the driver pulse and l_{med} is the interaction length.

Figure 10: Phase shifts as function of the argon pressure in a single 80 µm diameter jet for different intensities considering only atomic and plasma dispersion.

In the case dephasing is the dominated by free electrons, $l_{med} \cdot \Delta k$ scales with the free electron density N_e and the phasing term of Eq.(2.35) can be rewritten as

$$I_q \propto sin\left(\frac{l_{med} \cdot \Delta k}{2}\right)^2 = sin\left(\frac{\pi \cdot N_a}{2 \cdot N_{a,q}}\right)^2 = sin\left(\frac{\pi \cdot N_{q,norm}}{2}\right)^2, \qquad (2.36)$$

where $N_{a,q}$ corresponds to the density, where the q-th harmonic grows monotonically over the propagations distance l_{med}.

2.3.2 Absorption

In addition to phase matching, absorption can have a significant influence on the efficiency on the HHG-process. It depends on the XUV wavelength and the used HHG-medium, whether it is possible to attain pressures equal to one coherence length for efficient phase matching. Absorption effects can play a major role decreasing the harmonic yield before destructive interference by phase shifts sets in. The influence of the absorption on the harmonic can be defined as [34]:

$$I_q \propto N_a^2 \cdot \left[1 + exp\left(-\frac{l_{med}}{l_{abs,q}}\right) - 2\cos\left(\frac{\pi \cdot l_{med}}{l_{coh,q}}\right) \cdot exp\left(-\frac{l_{med}}{2 \cdot l_{abs,q}}\right)\right], \qquad (2.37)$$

where l_{med} is the target length and $l_{abs,q}$ is the wavelength specific absorption length. And is defined as

$$l_{abs} = \frac{1}{\alpha(\lambda)}, \qquad (2.38)$$

where α is the wavelength dependent absorption coefficient. The absorption length defines the distance where the intensity has dropped to 1/e.
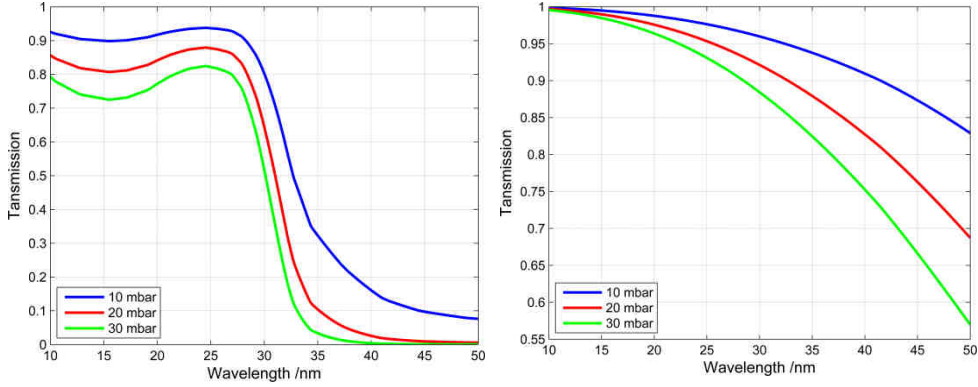
Figure 11: Transmissions curves for argon (left) and hydrogen (right) for a 250 µm gas jet at several gas pressures.

In [34] a rule of thumb has been defined for the basic conditions, in order to achieve phase-limited HHG in absorbing gases. This is the case, when the conditions $l_c > 5l_{abs}$ and $l_{med} > 3l_{abs}$ are given. At these conditions the gain of signal due to coherent superposition exceeds the absorption.

The wavelength dependent transmission of argon and hydrogen is shown in Figure 11 for several pressures. In the range between 35 and 50 *nm* the transmission of argon is strongly decreasing, which has the potential to suppress effective QPM-enhancement.

2.3.3   Critical ionization rate

In order to achieve a higher cut-off, higher intensity can be used. But increasing the intensity leads to higher ionization rates and will result in complete depletion of the ground state at intensity values higher than $10^{16} \, W/cm^2$. A complete depletion of the ground state suppresses the HHG-process, because the HHG driving tunnel current would be disrupted completely. However, before a complete depletion the ionization fraction reaches a critical value. The plasma dispersion term becomes larger than the neutral dispersion term for all pressures. Thus, phase matching is not possible anymore [35]. This critical ionization fraction can be derived from Eq.(2.33) is given by

$$\eta_{cr} = \left(1 + \frac{N \cdot r_e \cdot \lambda^2}{2\pi \cdot \Delta n}\right)^{-1}, \tag{2.39}$$

assuming q large, where the term proportional $1/q$ in Eq.(2.33) becomes small.

2.3.4   Plasma defocusing

Another limitation can occur, caused by plasma defocusing. Since the transverse intensity distribution of a Gaussian shaped laser is not constant, the ioni-

zation rate varies over the transverse profile of the pulse. The higher electron densities reduce the refractive index [36]. The resulting index gradient acts like a concave lens and leads to changes in phase and intensity. Plasma defocusing becomes especially important at high gas densities and high driver intensities [32].

2.4   Quasi-phase matching in free space geometry

Quasi-phase matching (QPM) is an approach in order to overcome the phase limitations of classical phase matching, which limits the interaction length and the maximal harmonic yield. QPM avoids interaction length limitation by utilizing a periodic structure in the nonlinear medium to correct for the phase-mismatch throughout the medium. This technique can improve the HHG-process in two cases.

i.   In the case of phase-limited HHG, where absorption effects and other limitations play a minor role, the resulting phase-mismatch prohibits an efficient HHG-process after one coherence length. The harmonic yield is oscillating with a period of $2 \cdot lc$. QPM can gain signal beyond the coherence length lc.

ii.   For the extension of the cut-off, higher intensities can be used. However, this leads to significant ionization rates and pressure-tuning becomes insufficient, when the critical ionization ratio is exceeded. The phase-mismatch cannot be corrected sufficiently. Thus, the coherence length significantly decreases so that conversion efficiency becomes low. Nevertheless, the QPM approach can compensate the low conversion efficiency. The constructive interference of several low harmonic yield emitters can lead to significant signal gain.

In both cases it is desirable to generate harmonics beyond the coherence length. In order to bypass the phase matching limitation, the HHG-process has to be suppressed in the regions, where destructive interference occurs. Thus, a periodic structure is introduced that, in the ideal case, allows phase-limited HHG in the first half (HHG-zone) of a period and suppress HHG in the second half. Next to the suppression the phase-mismatch has to be compensated (phase matching zone). At the beginning of the second period, the generated radiation can coherently superpose with the radiation from the first period. Under optimal conditions the signal depends on the squared number of QPM-periods N_{QPM}.

The spatial modulation for the periodic QPM structure can be created by modulating either driver beam intensity or atomic density. The modulation depth of the QPM structure is important for scalability in general and is demonstrated in Figure 12.
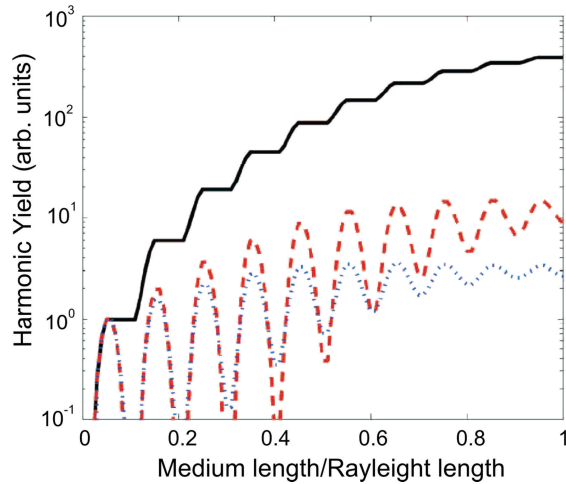
Figure 12: Characteristic ideal growth of the harmonic yield (black). Due to residual phase-mismatches the signal oscillates with multiple of the coherence length (red,blue). Furthermore, the non-ideal increase is two orders of magnitude lower than the ideal case. In the (blue) curve absorption is included and reduces the signal further [16].

The figure shows the signal growth of a 10 period QPM target with different modulation depths and an assumed phase shift of π between the HHG-zones. The target is in the focus of the driving field and the complete length of the medium is equal to the Rayleigh length.

The ideal QPM signal (black) with perfect modulation depth (rectangular function) shows a continuous signal growth. It is just interrupted by the phase matching zones. However, the perfect scaling is limited, because a rectangular modulation with a 100% modulation depth is not accessible under realistic conditions. The red curve shows the QPM signal for a sinusoidal modulation depth of 4%.

As already mentioned in the introduction, several different approaches have been developed to utilize the QPM technique. However, this thesis concentrates only on the atomic modulation in free space geometry, because a high average power is requested, which other techniques maybe cannot resist.

The density modulation technique in free space geometry (gas jet) uses several targets. Leadoff experiments have been realized using the vacuum phase-shift as phase matching parameter in vacuum intersections among multiple jets [14,15]. The phase matching mechanism is induced by separation of the gas jets. Since, the effect of the vacuum phase-shift is weak, the separations spacing has to be expanded in order to increase the phase-shift, which results in absolute length longer than in a realistic Rayleigh length of HHG-setup. As all targets need to be inside the Rayleigh length in order to obtain an approximately constant intensity level for all targets. Secondly, the focusing induces a geometrical phase-shift (Gouy-shift) within the Rayleigh length, which has to be compensated by additional spacing. For this reason the cumulated distance between the single targets for QPM limits the maximum number of QPM periods and the enhancement factor. To fulfill the request of a large number of jets

for a substantial signal improvement and high degree of coherent control the spacing between the single gas jets has to be decreased.

For this account the phase-shift has to be introduced with a more effective method by replacing the vacuum intersections with a dispersive medium. This medium has to fulfill following requirements.

1. Passive regarding to HHG
2. Controllable phase-shift
3. Insignificant absorption for driver-pulse and harmonic

On the strength of [19], which provided the basis information for the preparation of the experiment, hydrogen has to be fully ionized in order to fulfill these requirements as matching-medium. It develops at laser intensities $\geq 3 \cdot 10^{14} \, W/cm^2$ [16], which is a lower boundary of the usually used intensity range for the HHG-process. The fully ionized hydrogen cannot participate in the HHG-process. Additionally, the dispersion can be controlled via the pressure and hydrogen exhibits low absorption for high order harmonics. This makes it feasible to develop an alternating dual-gas target with the capability to adjust the pressure of HHG-gas and phase matching gas separately.

Proof-of-principle experiments for improving the harmonic yield by efficient control of coherence has been accomplished [17,38]. Additionally the control of the relative weight of long and short trajectories has been measured [17]. This allows controlling the atto-chirp of the plateau harmonics.

Eq.(2.36) describes the relation between harmonic intensity and atomic density of single jet geometry under the assumption the single atom response has the same amplitude for all emitters N_a. Additionally a linear dependency exists between the phase-mismatch Δk and free electrons N_e. With the same assumptions the paper *Seres et al.* [14] introduced an extension describing the harmonic intensity scaling for a multi-jet geometry in general. The phase matching zones assumed to be optimized to a phase shift of π.

$$I_q(N_{q,norm}) \propto \frac{1-(-1)^{N_{QPM}} \cdot \cos(\pi \cdot N_{q,norm})}{1 + \cos\left(\frac{\pi \cdot N_{q,norm}}{N_{QPM}}\right)} \sin^2\left(\frac{\pi \cdot N_{q,norm}}{2 \cdot N_{QPM}}\right) \qquad (2.40)$$

Figure 13 shows the plot of equation (2.40) and exhibits the harmonic intensity scaling for a single jet and a QPM target with 2 to 4 QPM periods. The harmonic intensity is plotted against the normalized atomic density $N_{QPM} = 1 \; to \; 4$. The plot shows saturation according to the equation (2.40) at $N_{q,norm}/N_{q,norm} = 1$, which correlates with the maximal enhancement of the N_{QPM}^2 dependence. This correlation and the plot itself are important for the experimental approach to
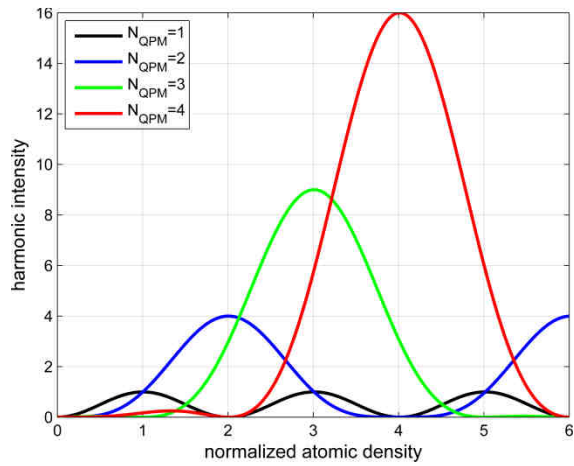
Figure 13: Behavior of the harmonic intensity regarding to the normalized atomic density of the HHG-medium for a single jet $N_{QPM} = 1$ (black) and three different QPM-period variations $N_{QPM} = 2\ to\ 4$ (color). The normalized atomic density of one creates a phase shift of π in a single jet configuration. For a multi-jet target a multiple of the normalized atomic density is needed to achieve optimal QPM conditions – cf. Eq.(2.40).

find optimal QPM conditions. Only the correspondent HHG-gas pressure allows gaining the expected significant enhancement by QPM.

3 1d-Simulation QPM-target

3.1 Performance range

As a preparatory step for the experiment, where the QPM target should be tested with pulse durations of $3.5\,fs$ and pulse energies of $400\,\mu J$, the phase matching characteristics of the target has been simulated numerically [22]. The aim of the simulation is helping to restrict the parameter range and find reasonable start values for target and laser parameters. To limit the computing time, the simulation has been calculated for one dimension only and beam propagation, plasma defocusing or self-phase modulation effects have not been considered.

Furthermore, the simulation has been developed for few-cycle pulses ($3.5\,fs$) in the first place. In this case, if ionization occurs, the degree of ionization is low and only defined by one or two cycles. In this case the time dependence of the ionization can be neglected.

However, in both realized experiment and simulation, laser pulses with a length of $500\,fs$ have been used. Here several hundred optical cycles generate high harmonics. The results of the simulation show significant impact on the ionization fraction in argon. A maximal ionization fraction (of the number of atoms) of 33% has been calculated – cf. Eq.(2.11) - for an intensity of $2.3 \cdot 10^{14}\,W/cm^2$. In this intensity regime even small variations of the intensity have a strong impact on the ionization fraction. Furthermore, the time dependent ionization fraction becomes elementary - cf. Figure 6. The average ionization level Z* is close to the ionization fraction η, because in this intensity regime the probability of multi ionization is close to zero.

At the same time the phase matching conditions are changing within the pulse. To calculate intra cycle phase matching conditions is both time-consuming and disproportional compared to the other simplifications. Since the high-order harmonics in the range of the cut-off are in the center of interest, the maximal ionization fraction is used as a static value for the calculations. For the pulse parameters $500\,fs$, $400\,\mu J$ and peak intensities of $2.3 \cdot 10^{14}\,W/cm^2$ ionization fraction (of the number of atoms) of over 30% has been determined - cf. Eq.(2.11). This order of magnitude makes it difficult to phase-match high-order harmonics, because the critical ionization level is exceeded.

Due to the strongly varying transmission curve, in the probed wavelength range, absorption effects in hydrogen and argon have been considered. Thus, the simulation bases on rudimentary assumptions, the conclusions of the results have only a qualitative character concerning the phase matching process. Conclusions about the absolute conversion efficiency cannot be drawn.
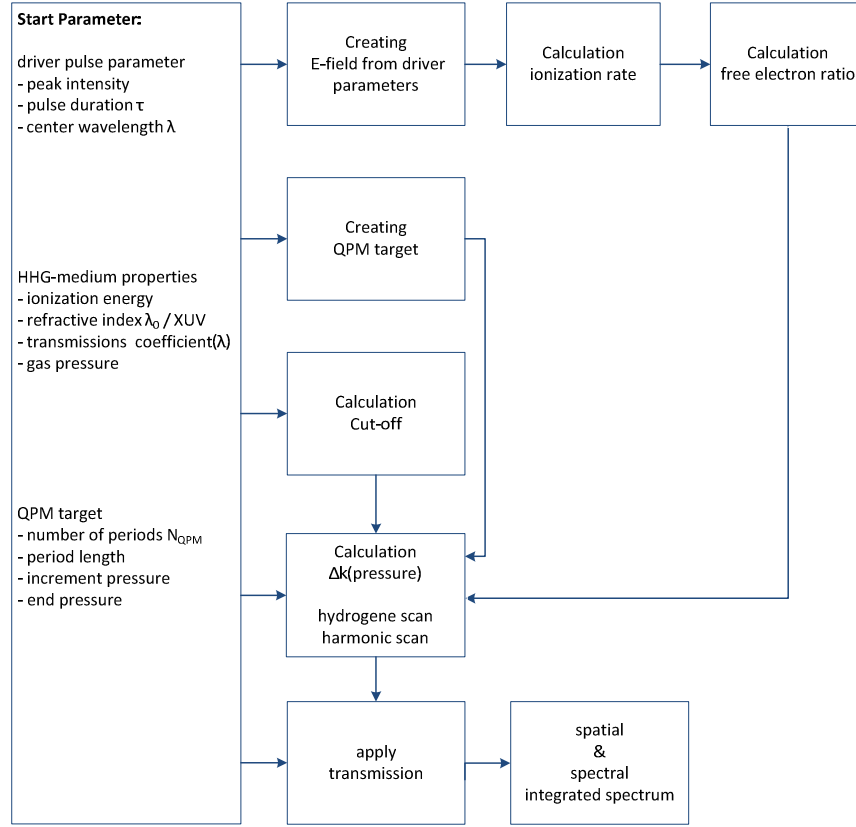
Figure 14: Flow chart of the 1-d simulation of the dual-gas QPM target.

A flow chart of the program is shown in Figure 14, which outlines the structure. For a given driver pulse (Gaussian shape) and medium the ionization rate is calculated by tunnel rate Eq.(2.10) and leads free electron ratio Eq.(2.11).

A 2D loop structure operates the hydrogen/harmonic scan to calculate total Δk Eq.(2.33) considering: normal dispersion for the HHG gas, plasma dispersion for both HHG-gas and hydrogen (fully ionized $\eta = 1$) and the Gouy-shift for one period. The relative QPM-signal is gained by applying the equation

$$I(q,j) = \left| \sum_{j=1}^{j_{max}} N(j) \cdot e^{-2i\Delta k(j,q,p)l_{jet}} \right|^2 , \qquad (2.41)$$

where N is the gas density, q the harmonic order, j_{max} the number of periods and l_{jet} the length of the jet. The equation is adapted from multimode beating QPM [11].

For a given laser intensity the cut-off harmonic is calculated, in order to define an exit condition for the loop operating the harmonic scan. Pressure range and resolution are entered for the scan manually. The absorption is calculated considering the target length and pressure. Furthermore, the residual gas pressure is estimated and distance to the detector is defined by the setup. The resulting
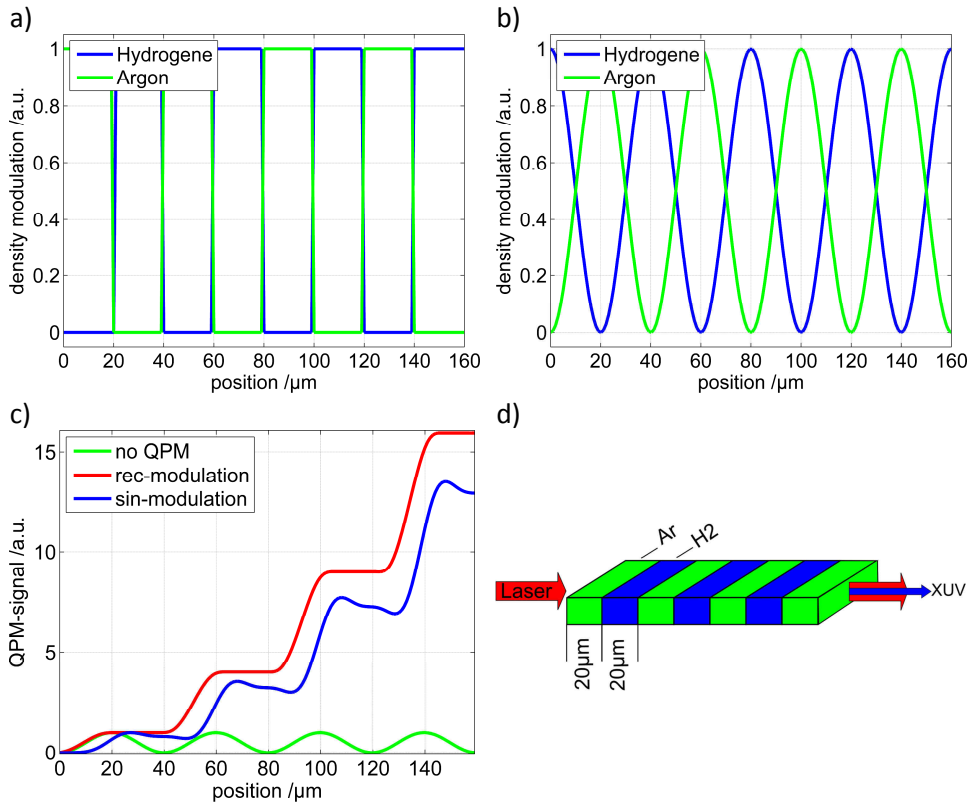
Figure 15: Modulation of the gas jets : a) rectangular. b) Sinusoidal. c) Optimized QPM-signal of the 37th harmonic plotted against propagation range for a QPM target ($N_{QPM} = 4$) with argon and hydrogen jets length of 20 µm each and different modulation shapes. Constructive interference occurs in all HHG-zones and leads to significant enhancement factors, which is related to the modulation form. d) [16] schematic overview of a dual gas QPM-target.

QPM-signal is plotted in arbitrary units against hydrogen pressure and wavelength at a given HHG-medium pressure.

The target model is described by a rectangular modulation function to simulate the periodic structure. Any other modulation can be implemented, but the rectangular one allows reducing the number of calculations for the propagation dimension down to the numbers of periods, although a rectangular structure is certainly not a realistic one – cf. Figure 18.

However, to compare rectangular (Figure 15a) and overlapping sinusoidal modulation (Figure 15b), the QPM-signal of the 37th harmonic was calculated spatial resolved. The evolving signal for both modulations is plotted in Figure 15c. As described in chapter 2.4 the maximal harmonic yield drops, because the divided generation and phase matching zones are smearing and the effective interaction length decreases.

3.2   Results and Conclusions

The Figure 16 exhibits the results of four hydrogen scan at varying argon pressures for the given pulse parameters $500\ fs$, $400\ \mu J$ and peak intensities of $2.3 \cdot 10^{14}\ W/cm^2$. In 16a (40 mbar) a reasonable signal has been gained with
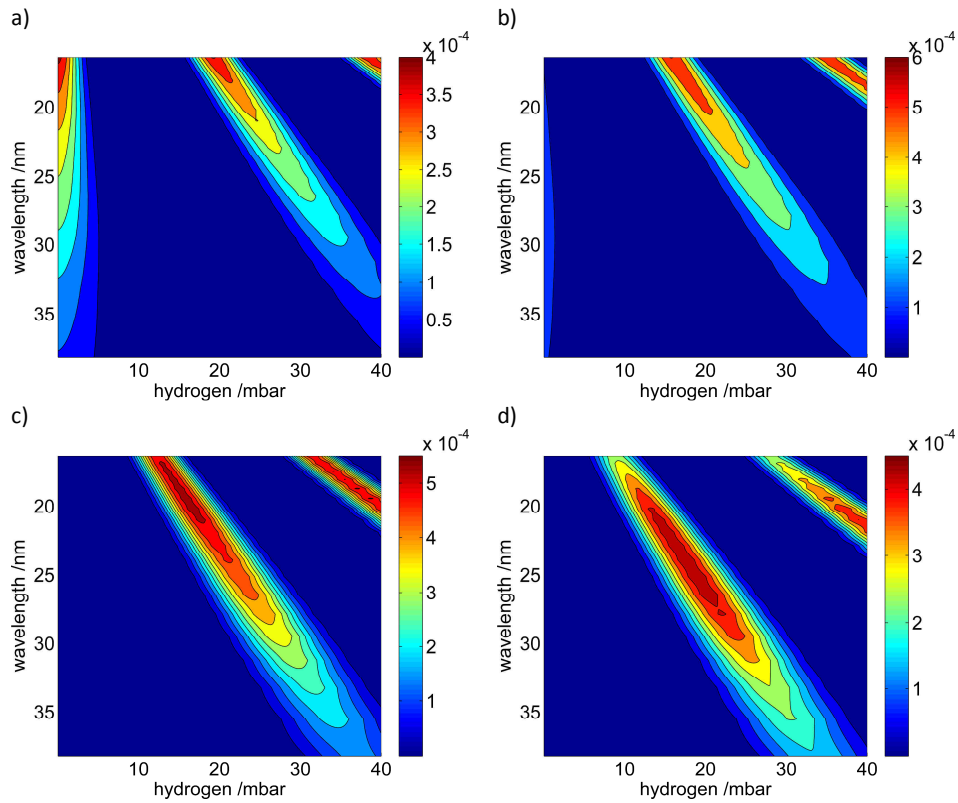
Figure 16: Results for the simulated hydrogen scan pressure in a dual-gas QPM target with $N_{QPM} = 4$ QPM periods. The contour diagram gives information about the intensity (arbitrary unit) related to wavelength and the hydrogen pressure for four different argon pressures: (a) 40 mbar, (b) 60 mbar, (c) 80 mbar, (d) 100 mbar with the given pulse parameters $500 \, fs$, $400 \, \mu J$ and peak intensities of $2.3 \cdot 10^{14} \, W/cm^2$.

out hydrogen. This is possible because the pressure induced coherence length is too long and constructive interference can occur over the whole target. The actual hydrogen scan leads to a dephasing first, which suppresses the signal. At 20 mbar hydrogen pressure the constructive interference sets in again. At this argon pressure the target acts like a single jet and no effective enhancement can be realized.

The argon pressure has to be tuned to higher pressures in order to generate phase-limited harmonics in each jet, which are needed to achieve optimal signal growth in all zones (cf. Figure 15). In 16b-d hydrogen scans are shown with argon pressures from 60 to $100 \, mbar$. It can be observed that the argon pressures generate a phase-limitation, which can be corrected by the hydrogen phase delay and improve the signal significantly. The phase matching area is tilted, because of the wavelength related refractive index in gases. Thus, the enhancement is wavelength dependent as well. For a given argon pressure, the enhanced wavelength ranges can be selected by setting the hydrogen pressure.

In order to maximize the signal for certain wavelength, the argon pressure has to be adjusted too. In 16b-d it is clearly visible, that the maximal signal output

shifts to higher wavelength with growing argon pressure. Simultaneously, the phase matching area moves to smaller hydrogen pressures. The behavior in the results of the simulation indicates that the dual-gas target allows independent control about both the enhanced wavelength range and the maximization of the enhancement

4 Experimental Setup

4.1 High repetition rate driver laser system

Although fiber lasers can produce high average power, in the kW regime, when operated at continuous wave mode [39], the amplification of ultrashort pulses to the mJ-level is a challenge. Pulsed fiber lasers tend to suffer intensity related non-linear effects, mainly self-phase modulation, which distorts the pulse structure. In general nonlinear effects are more dominant in fiber amplifiers than in other amplification schemes, because of the guidance of high intensities in small cores in long fibers (up to one meter). These effects have been reduced successfully by lowering the peak intensity applying the chirped pulse amplification scheme [40]. Additionally, novel large mode area structured rod-type photonic crystal fibers lead to lower peak intensity in the fiber, allowing single mode guidance in spite of the large mode field diameters of the fibers [41]. A combination of both technologies offered the development of a new class of high average power amplifiers producing $870\ fs$ pulses of up to $\sim 1\ mJ$ at $100\ kHz$ [21].

For the present dual-gas QPM experiment a fiber chirped pulse amplification (FCPA) system was used. It was capable of generating $80\ \mu J$ pulses at $1\ MHz$ repetitions rate with a duration of $580\ fs$ and central wavelength of $1030\ nm$ [42]. The system design, based on a modified version of the one described in [21], is shown in Figure 17. Additionally, a pulse shaper was integrated before the amplifiers in order to pre-compensate nonlinear phase changes, which accumulates in the main amplifiers [43]. The shaping device allows shortening pulses to less than $600\ fs$.

Complete ionized hydrogen is needed as phase matching medium in the QPM target. For this reason intensities $\geq 2.3 \cdot 10^{14}\ W/cm^2$ are required to completely ionize the hydrogen. At the same time the Rayleigh length needs to be larger than the target to achieve an approximately constant intensity level within the target. In order to achieve the required intensity, the $80\ \mu J$ pulses must have been strongly focused. However, this would have resulted in a too short Rayleigh length compared to a realistic target length of a couple of $100\ \mu m$. For this reason the pulse energy had to be increased. In order to do this, the repetition rate had to be re-
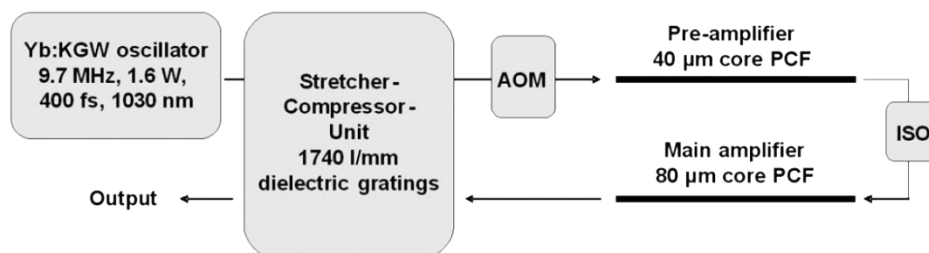

Figure 17: Schematic of the mJ level high repetition rate fiber CPA system. ISO, optical isolator; AOM, acousto-optical modulator; PCF, photonic crystal fiber. [21]

duced to $75\ kHz$ for several reasons: the average power was limited by the pump diodes, which cannot scale arbitrarily.

The higher peak power induces larger nonlinear phase shifts in the fiber. The phase shift leads to distortions of the temporal shape. In the temporal profile it evolves sidelobes next to the main pulse, which are so called satellite pulses [21]. Higher peak intensities in the amplifier would have generated distinct satellites, which are able to pre ionize the target medium. Argon ions are not able to participate on the HHG-process. Furthermore, a damage threshold limits the pump peak power to fiber specific values. All these conditions limited the maximum pulse energy to $400\ \mu J$. In contrast to the publications the pulse could only be compressed to $585 \pm 15\ fs$. With the limited pulse energy and duration available in this experiment, made it necessary to choose a tight focusing geometry to realize peak intensities $\geq 2.3 \cdot 10^{14}\ W/cm^2$ and accept reduced phase matching ability induced by strong influences of Gouy-shift and the inhomogeneous intensity distribution along the propagation direction. A sub-10 fs system, which was not available at that time, would have relaxed the focusing problem. The already tested sub-10 fs system [44] would allowed a loose focusing geometry at sufficient peak intensities.

4.2 The dual-gas foil target

The harmonic yield of an ideal QPM layout with isolated driving and phase matching zones is limited only by gas properties like absorption length, single atom response or binding energy. The phase matching zones should be passive concerning HHG to avoid destructive interferences with the argon harmonics. This allows tunable control of the phase between the separated sources at the same time and leads to an exact trajectory selection and rapid growth of the HHG signal. The matching medium should have negligible absorption for both harmonic and laser fields, otherwise it would reduce the efficiency of the target – cf. Figure 12. Another important parameter is the modulation depth of the QPM periods – cf. Figure 12 and Figure 15.

High intensities, required for HHG, can only be achieved around the focus in the Rayleigh range of the focused driver laser. To enable the maximum number of QPM periods the period length has to be as small as possible, and at the same time the total target length has to be shorter than the Rayleigh length, to avoid larger intensity changes and reduce the influence of the Gouy-shift.

Furthermore, high average power occurs with the usage of high repetition rate driver lasers. A HHG-target has to resist high peak powers and a high thermal load to be long lasting. This criterion makes free-propagation QPM schemes the most acceptable solution. Guided capillaries schemes may not work in this parameter range of high average power applications, although the mentioned techniques produced good results at lower repetition rates [45].
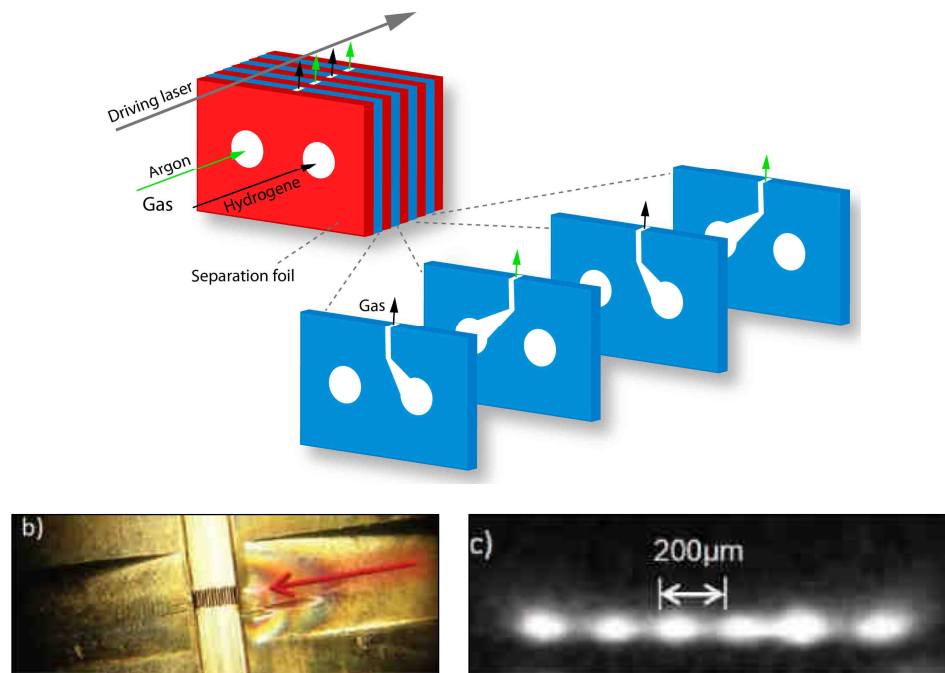
a)

Figure 18: Scheme of the foil target design. a) Stacked steel foils with two separated channels for HHG and phase matching gas (both 50-100µm thick, blue). The foils are flipped alternating to create the periodic structure. Between the alternating jets a separation foil is inserted (20µm, red). b) Top view of the compressed foils n the target holder. c) Image of the plasma generated by six alternating argon and five hydrogen jets. Two additionally hydrogen jets are enclosing the generation medium at the front and end of the array. [18]

In order to fulfill all requirements, a novel QPM-multi-jet design has been developed [16], in which a HHG medium alternates with hydrogen as passive matching medium. The pressure of both zones can be set separately, in order to allow a continuous modulation depth.

Figure 18 shows that the target design is based on a stack of steel foils with rectangular nozzles and two feed channels, which are alternating in orientation. To resist the high peak and average power, all foils are made of steel. The two channels allow independent pressure control of HHG and phase matching zone.

To preserve a high contrast between the generation and phase matching gas, 20 µm separation foils divides the feed lines, but with holes for the main channels. The separation allows a parallel flow of the gas jets which leads to less turbulence in the intersection areas.

The hydrogen and HHG jets are set very close to each other to achieve distinct zones with a sharp contrast. This is necessary to create a deeply modulated density, which is a key parameter for ideal QPM enhancement (cf. Figure 15). Additionally, the array should start and end with a hydrogen jet, which will have no effect on the phase matching, but improve the geometrical boundary for the spreading density of the generation medium.

The dual-gas target used for the experiment had several stages of development. The first version was not scalable to higher jet numbers and consisted of complicated Laval-nozzle design [16]. These nozzles created turbulences in the interaction zone, because of the crossing angle between HHG and hydrogen jet. In the recent version several improvements increased the flexibility of the target in the sense of both number and size of the jets.

It can be necessary to carry out measurements in a pulsed mode to limit the average gas load in the chamber. This prevents overload of turbo pumps in the setup and avoids a high background pressure in the chamber, which leads to absorption effects. The electro pneumatic valves (Parker no. 9S1-A1-P1-9B06), which switches on/off the gas flow for both main feed lines are directly mounted on the holder system. In order to keep the volume small between valve and nozzle exit, the valves are close to the array for two reasons. First, a big volume after the valve would reduce the gas pulse contrast. Second, to pump bigger volumes through the small cross section of the jet would extend the pump time of the residual gas when the valves are closed already. This increases the time cycle of a measurement.

4.3 HHG-Setup

Since XUV-radiation is strongly absorbed in air ($l_{abs} \approx 10 \ \mu m$), the experiment has to be accomplished under vacuum conditions. A schematic of the experimental setup is shown in Figure 19. The vacuum in the experimental chamber is maintained by a turbo pump and a scroll pump as roughing line. Additionally a roots pump could be used parallel to the turbo pump in case of high gas loads.
The target is mounted on a motorized 3-axis manipulator and can be moved with µm resolution. On the exit side the target is connected to a membrane bellow to an exhaust pipe. The mounting reduces the operating range in beam direction to $\pm 15mm$. A scroll pump directly pumps the exhaust pipe. The jets are pointing into the direction of this exhaust line to reduce the gas load in the chamber.

The Parker valves, which operate the jet flow, are independently connected to external controllers. An internal cycle unit manages the valves on/off timings. Each cycle can be triggered externally, which allows automatized measurement, which is important to carry out pressure scans. The backing pressure for each jet type independently can be controlled with mbar resolution up to maximal pressure of 7 bars (MKS Instruments 640 Absolute Pressure controller). Since the flow of the controllers is limited, the backing pressure cannot be kept constant in the target at higher set pressures. To avoid pressure drops during a measurement a gas reservoir is interconnected between each controller and valve pair. This allows an integration time of $> 0.6 \ s$, in which the backing pressure drops less than $20 \ mbar$.

Figure 19: Schematic of the experimental setup for accomplishing automatized pressure scans in order to find optimal QPM pressure conditions.

The driver beam generated by the FCPA described in chapter 4.1 is coupled into the experimental chamber and focused by a $75\ mm$ focal length lens into the target where the harmonics are generated. After propagating through the chamber the fundamental and harmonics are separated by a thin aluminum filter before the spectrometer. The filter is attached directly to the slit to improve heat transport between filter and water cooled slit holder. This extends the lifetime of the aluminum filters at high repetitions rates. The slit holder is also motorized and can be adjusted externally. For spectral resolved detection of the high harmonics a flat field grazing-incidence (Hitachi, 1200 lines/mm) spectrograph (Ultrafast Innovations) in combination with spectroscopic CCD camera as detector (Andor Newton 940P-BN 2048x512) is used.

A LabView program allowed carrying out automatized pressure scans in a preset parameter range (start pressure, end pressure, increment) with argon and/or hydrogen to find the optimal phase matching conditions. The program first sets the pressure and waits till the set pressure is reached. Then a signal is created by a multifunction's DAQ card (NI-6009). The signal triggers the valve controllers and, after 100μs delay the camera is also triggered. The delay is necessary to ensure that the gas jet is fully developed. Additionally, the jet time last $100\ \mu s$ longer than the exposure time to avoid blurring effects due to pressure fading while the measurement. In the operating software (Andor Solis) of the camera the exposure time (0.6s) and pixel binning (1:4) is set. The operating software organized the read out and sequential data storage.

4.4 Commissioning

Before starting the actual experiment, the whole experimental setup had be commissioned. The most difficult part of the commissioning process was the generation and detection of the first harmonic signal, because of the high number of degrees of freedom in the experimental setup and the small size of the target.

In the first step, the focusing optic had been chosen in consideration to existing laser parameters (chapter 4.1), required intensity and Rayleigh length. In these experiments, the pulse energy and pulse duration of the laser system have been less than expected in the planning phase. For this reason a tight focusing geometry was needed to achieve sufficient peak intensity.

The intensity has to be $\geq 2.3 \cdot 10^{14} \ W/cm^2$ to fully ionize the hydrogen. This was actually a problem, because the choice of the focal length is also restricted by the flange/wall of experimental chamber. The lens was therefore positioned inside the chamber in order to reach the intensity level. For the given beam parameters and a $75 \ mm$ focal lens an intensity of $2.33 \cdot 10^{14} \ W/cm^2$ was calculated. However, the small Rayleigh length of $340 \ \mu m$ was limiting the number of QPM-periods. With the prepared $100 \ \mu m$ target foils only two periods have been realized. At a later time $50 \ \mu m$ foils have been available, which allowed a four period target.

In the second step the unamplified driver beam was coupled into the experimental chamber to avoid damage during the alignment. The beam was aligned parallel to the table surface, passing the filter holder and intercepting the grating in the center and parallel to the row of hole along the propagation axis. For this procedure the camera was dismounted and the filter extracted in order to see the scattered light on the grating with an infrared viewer. Two irises, one before the entrance window and a second iris before the filter holder in the chamber, reproduce the propagation axis after the alignment. Since there were no rotary stages to correct the angle orientation of the target, the hole pattern of the optical table define the orientation. The precision of the target orientation to the beam axis could not be measured or optimized by beam manipulation on the HHG signal later, because of the lens characteristics. An adjustment of the driver beam would always affect direction and position of the beam. Already small changes led to clipping at the aperture behind the filter holder.

The focus lens was inserted after the target had been moved out of the beam. The lens was centered and the focal plane was aligned perpendicular to the beam axis. Although the beam was strongly diverging after the focal plane, the second iris was used to check the lens alignment. For the next commissioning steps higher peak power has be needed in order to generate plasma in air.
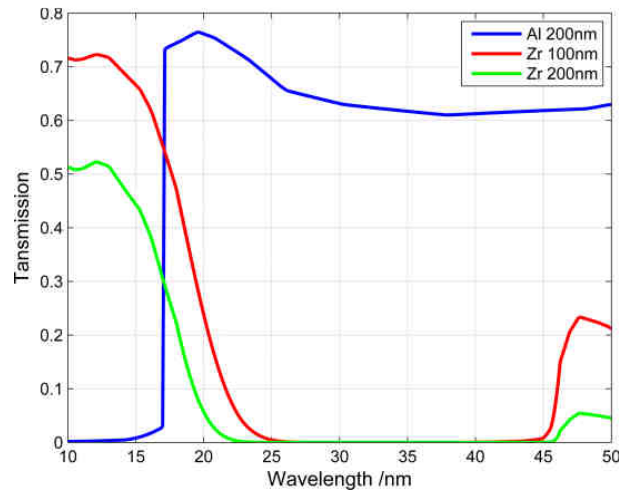
Figure 20: Spectral transmission curve for aluminum and zirconium filter.

The pulse energy had been increased until plasma was observed in the atmosphere. The plasma was a good indicator for the focal plane of the lens and is used as initial position of the target. The viewing slot on the top side of the target allows monitoring the interaction area, while the nozzle exit is moved close to the plasma.

Before the chamber can be closed it should be checked if the electro pneumatic valves are operating properly. The initial pump down has to be carefully controlled, because the rough pumping, performed by the scroll pumps, induces a strong flow at atmosphere pressure. This flow can destroy the sensitive aluminum filters. The flow is reduced by manual valves till the base pressure reaches the low mbar range. The turbo pump is switched on at a chamber pressure below $2\,mbar$.

After reaching the maximal pump speed, the pulsed argon injection is started at 2-3 bar backing pressure and the laser pulse energy is increased to $400\,\mu J$. In the case that the target gas is not ionized, it is reasonable to move the target in an iterative procedure (x,y,z) to a position, where the plasma plume appears. The volume, where the plasma can be induced, defines the coordinates for the HHG-signal retrieval. The volume has to be scanned in $15\,\mu m$ steps till a spectrum can be detected with the spectrometer. While the target scan gas and laser parameters are continuously cross-checked, to make sure harmonics can be generated. The movement has to be controlled with precaution in order to prevent ablation of target holder. Ablated particles can condense on the lens and lead to transmission losses. At the high repetition rate, the lens would be heavily coated within seconds.

In principal it would have been easier to find a signal while looking on the direct XUV beam. Furthermore, the beam profile gives information about the path of the driver beam through the medium in general. However, the spectrometer geometry did not allow a direct observation of the beam. For this

37

reason the alignment was only optimized by considering the spectrally resolved harmonic yield.

In the next step, the view field of the camera was optimized. The camera position is tuned to a position where the grating images the spectrum with approximately $14\,nm$ wavelength as the lower boundary. The aluminum absorption edge at $17\,nm$ was used as an indicator for the wavelength calibration - see Figure 20. Oxide layers are not considered. An energy calibration would have been necessary to obtain absolute photon counts. The calibration curve depends mainly on the aluminum filter transmission, grating efficiency and quantum efficiency of the detector. The absolute photon counts are important to compare targets characterized in different experimental setups. In this case only the relative changes of the signal, while a pressure scan, matter, therefore energy calibrations have not been accomplished.

5 Experimental Results

5.1 Experimental procedure

The main goal of the performed experiment was the characterization of the possible enhancement of HHG-efficiency by applying QPM dual-gas target at high repetition rates. The target was studied at given driver laser parameters: $75\ kHz$ repetition rate, a peak intensity of $\geq 2.3 \cdot 10^{14}\ W/cm^2$ and a center wavelength of $1030\ nm$, regarding to the two core questions:

    i.   How large is the effective enhancement factor?

    ii.   Is it possible to extend the cut-off toward higher photon energies?

In order to establish the optimal working conditions to accomplish sufficient QPM, the dual-gas target has to be experimentally characterized in inert gas only, which simulates a single-jet target. It is essential to find the specific HHG backing pressure $p_{\pi,\lambda}$ introducing a phase-shift of π or rather a multiple of it. As described before, the theoretical QPM enhancement factor $N_{QPM}{}^2$ can only be observed, if the absolute phase-shift is equal to π in each jet of the multi-jet target (cf. Section 2.4). The absolute phase-shift induced by the HHG-medium in the complete target has to be $N_{QPM} \cdot \pi$ (cf. Figure 13).

To determine the specific pressure $(p_{\pi,\lambda})$ introducing the favored phase-shift at a spectral region, the spectrally resolved harmonic yield has to be measured as a function of the argon backing pressure (argon pressure scan). The specific roll-over backing pressure is – together with the harmonic wavelength - related to several parameters: HHG-medium, driver laser intensity, focusing geometry and number of jets. Each change in one of these parameters modifies the phase matching conditions. At the same time the tuning behavior of the pressure induced phase-shift changed – cf. Eq.(2.29).

The observation of pressure related oscillations in the harmonic yield indicate the phase-shifting. The first peak of an oscillation (roll-over) correlates to a phase-shift of π and defines the specific pressure $p_{\pi,\lambda}$. In theory $N_{QPM} \cdot p_{\pi,\lambda}$ corresponds to the pressure needed for the maximal QPM enhancement. Nevertheless, the scan has to be performed to the second roll-over at least, in order to prove that the first roll-over is induced by phase effects and not by absorption due to higher gas densities. Furthermore, the strict periodicity of the oscillations in theory is not necessarily given in experiments, because of the multiple parameter dependence of $p_{\pi,\lambda}$.

Another fundamental problem complicates the detection of the phase oscillations. Under experimental conditions, 3-D and time domain effects blur the contrast of the spectral resolved signal within a pressure scan. The not constant intensity distribution of the driver laser in space and time (multi-cycle characteristic) leads to different phase matching conditions the intrinsic related $p_{\pi,\lambda}$ in space and time. Since the measurement integrates the harmonic yield in both spatially and temporally (intra pulse) dimension, the signal trace represents -strictly speaking- just an averaged phase matching effect. For this reason a distinct peak as a roll-over cannot be detected mandatorily. Changes in the slope within a pressure scan can be an indication for a roll-over.

Nevertheless, after determining the wavelength-dependent roll-over pressures, the actual QPM-experiment can be accomplished. At constant HHG-gas pressure, corresponding to a chosen spectral range, a hydrogen scan has to be performed. The ionized hydrogen introduces a phase-delay with increasing backing pressure. Approaching a pressure corresponding to a phase shift of π in each hydrogen jet (phase matching zone), the constructive superposition of the harmonics increase the harmonic signal. The roll-over in the harmonic signal indicates the desired phase-shift of π in the phase matching zones. Under ideal circumstances the harmonic yield can be enhanced by the factor of $N_{QPM}{}^2$ compared to a single target (e.g. classic nickel tube [46]) of the same length.

In the dual-gas QPM approach the complete ionization of hydrogen is important and defines the lower boundary for the intensity. Before first HHG-medium scans are performed a pure hydrogen scan has to proof that the hydrogen does not create harmonics. Strong harmonic generation in the phase matching zone would invalidate the QPM approach by destructive interference.

Argon was chosen as HHG-medium, because it has an efficient single atom response and sufficient transmission characteristics in the probed wavelength range. The results presented and discussed in the next chapter are divided in argon and hydrogen scans.

5.2 Argon pressure scans

In order to generate effective QPM harmonics, the target was characterized concerning the specific phase oscillations in the HHG-medium mode (only argon). Therefore, argon scans were performed at the beginning of the experiment and after major changes in the critical parameters (alignment, intensity). The behavior of the laser system and the tight focusing geometry introduced complications regarding to the distinct determination of the specific roll-over pressures $p_{\pi,\lambda}$. The gained knowledge of the influence of the laser and the focusing are presented separately before the actual determined roll-over results.

5.2.1 Laser pulse energy fluctuations

In Figure 21 an exemplary argon scan from 1 to 7 *bars* is shown for five different harmonics. The background corrected and both spatial and spectral integrated intensities (FWHM) of each single harmonic of the observed spectrum are plotted against the argon backing pressure. For the background determination, a Gaussian curve was fitted to the raw data of each single harmonic. The fit parameters within the 95% confidence interval were used to determine the uncertainty of the data analysis. The determined uncertainty is indicated in the error bars - see Figure 21.

The Figure 21 exhibits fast fluctuations in the pressure scan curves, which have been observed within the complete scan. Since the determined uncertainty is smaller than the amplitude of the measured fluctuations, they cannot be artifacts of the data analysis, but have to be induced by changes in the pressure or in the laser intensity.

At the beginning of the experiment the exact origin of the fluctuations was unknown and led to misinterpretations in several aspects. Driver laser fluctuations with amplitude of this order have to be clearly visible in the HHG-spectrum, because the cut-off wavelength has to vary with changing driver laser intensity (Eq.2.1). Accordingly, the cut-off could not be observed, because of the absorption edge of the aluminum filter – see Figure 20. In the ongoing experiment a correlation between the fluctuations and the cooling system was established. The fluctuations were induced by periodic oscillations in the pulse energy of the main amplifier.

The period time of the temperature oscillations was approximately 20 *s*. Due to the waiting time of the pressure tuning in between two pressure steps, which also was not constant, the recording speed was too low in order to reconstruct the oscillation in the measured data. Therefore, the oscillations appeared in the signal only as random fluctuations.
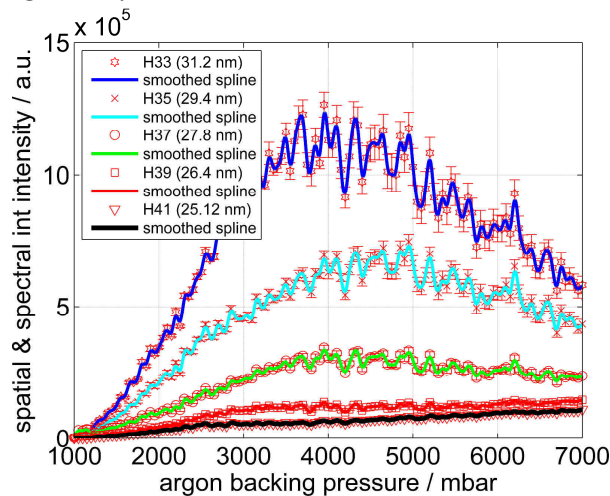
Figure 21: Spatially and spectrally integrated harmonic yield plotted as a function of the argon backing pressure for selected harmonics (31,29,27,26,25 nm). The plot gives information about the specific roll-over pressure, which corresponds to a phase-shift of π and is needed to accomplish QPM.

The origin of the driver pulse energy oscillations was the large temperature hysteresis of the pump diode cooling system. The hysteresis, defined by the temperature control unit, could not be changed. The spectral emission of a diode is related to the temperature (semiconductor band gap changes with temperature). The change of the center wavelength modifies the optimal in-coupling parameter for the photonic crystal fiber, which is the centerpiece of the main amplifier. As a consequence the pump pulse was fluctuating and affected directly the pulse energy and the intensity in the experiment. However, the problems connected to the cooling system could not be solved within the experimental time.

The energy fluctuations influence, next to the cut-off variation, the ionization ration and the related phase matching condition (cf. Figure 10). The amplitudes of the fluctuations are larger close to the peak. Fluctuating phase matching condition are unfavorable for stable QPM, because there influence can be even stronger.

5.2.2 Large free electron density effects

Large intensities in combination with high gas pressures lead to large electron density in the interactions zone, which can distort the HHG-process. The intensity is related to the driver pulse, the focus geometry and the alignment. At a given pulse and focus geometry, the focus position (alignment) is the only adjustable parameter for the intensity. When the focus is centered in propagation direction on the target, the ionization level is maximized.
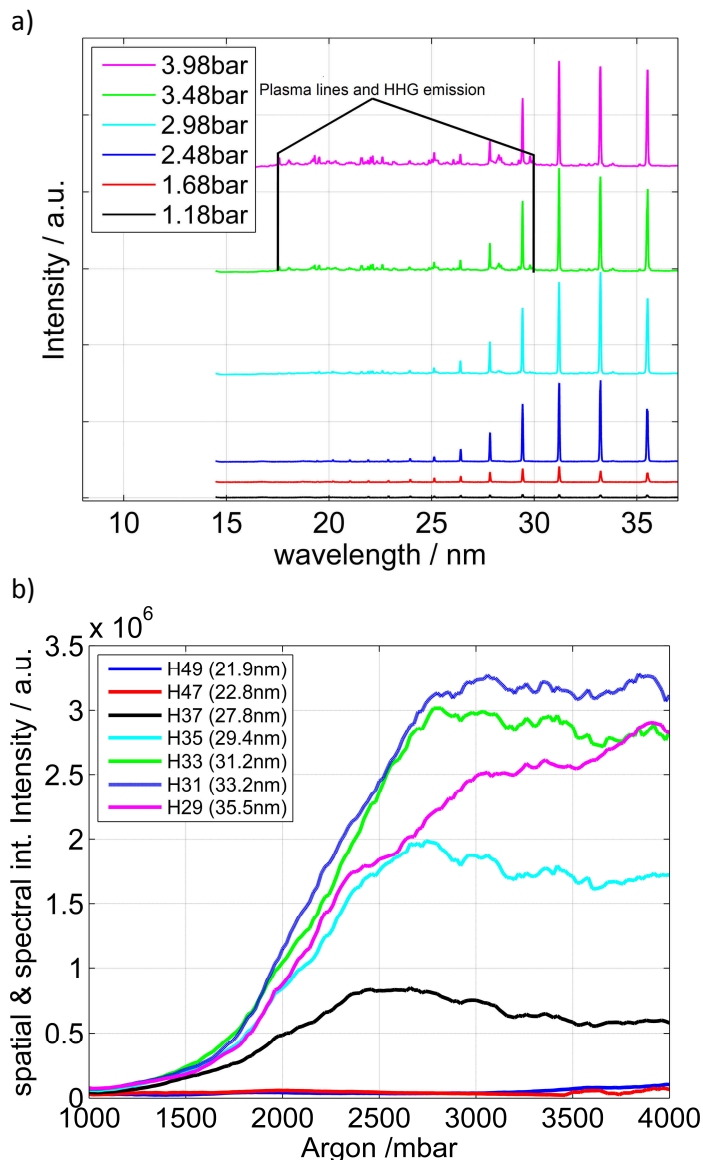

Figure 22: The Target: 4 x 50µm argon jets. Scanning range: from 1 to 4 bar Argon backing pressure. Focus: centered on the target in z-direction. The pulse energy was 400 µJ and the pulse duration 570 fs. a) Qualitative overview of the spectral development of an argon pressure scan. Large free electron density favors the development of plasma lines (atomic transition emission) between 17 and 30 nm. This effect is mainly related to the focus position. b) Plot of the spectrally integrated harmonic yield against the pressure. The low order harmonics in the spectrum suffer saturation effects as well due to large free electron densities. For a clarified overview a smooth filter was applied in order to attenuate the fluctuations.

In order to maximize the QPM-periods within the Rayleigh-length, the jet structure was made smaller and $50\ \mu m$ foils were used for the first time in this experiment. Due to the minimization of the jet length, the densities have to be increased at the same time, so that the harmonic yield stays constant and phase limitation can be obtained.

In Figure 22, visualizing both spectral shape and harmonic yield related to the backing pressure, two effects are visible, which are both related to the large free electron densities in the HHG-medium.

First, the harmonic yield saturates between 2.5 to $3\ bar$ argon backing pressure – see Figure 22b. Secondly, above the saturation pressure spikes are rising in the HHG spectrum – see Figure 22a.

The spikes in the spectrum are laser induced plasma emission lines, caused by atomic transitions. Bright plasmas are favored by high intensities. This regime is unfavorable to HHG because of ionization saturation and phase matching effects due to the free electrons generated [47]. In [47] the appearance of plasma lines and high harmonics are observed at the same time and the plasma lines are used for wavelength calibration. As well the saturation behavior can be traced back to a high free electron density. The large electron densities induce plasma defocusing – cf. subsection (2.3.4). However, the phase matching mechanism and plasma defocusing cancel out each other and lead to a saturation in the harmonic yield at certain pressures [29]. Previous studies [37,48] showed plasma defocusing effects in neon at peak pressures in the range of $80\ mbar$ and at intensities of $6 \cdot 10^{14} W/cm^2$. They calibrated the actual pressure in the interaction zone with an interferometric density measurement. However, the exact density and intensity conditions are unknown in the interaction zone for this experiment.

More relevant for the plasma defocusing are the gas densities, which are increasing proportionally with backing pressure. The actual pressure (density) conditions are target specific and have to be obtained by an interferometric gas density profile measurement. Additionally, the free electron density of the plasma can be measured. In both cases, neutral atoms and plasma, the refractive index is related to the density and can be obtained with a Michelson [49] or Mach-Zehnder [50] interferometer for example. This will be performed in future studies. For more information see [51].

Usually the cut-off wavelength gives a good approach to determine the intensity considering the cut-off law in Eq.(2.1). In Figure 22a the high-order harmonics are suppressed, because the critical ionization level is exceeded. The cut-off in this figure is limited by phase matching limitations, therefore it cannot be used to derive the intensity.

5.2.3 Influence of the focus position

In general, a tight focusing geometry does not only make the alignment more sensitive, but it also limits the phase matching capability of the pressure tuning in general [52], because this geometry tends to exceed the critical ionization (intensity) and the influence of the Gouy-shift becomes stronger - cf. Eq.(2.33). Both effects can be modified by shifting the focus position. To illustrate qualitatively the influence of the focus position in this setup, the pressure scan at two different focus positions was performed. Figure 23a and the Figure 24a

a)

b)
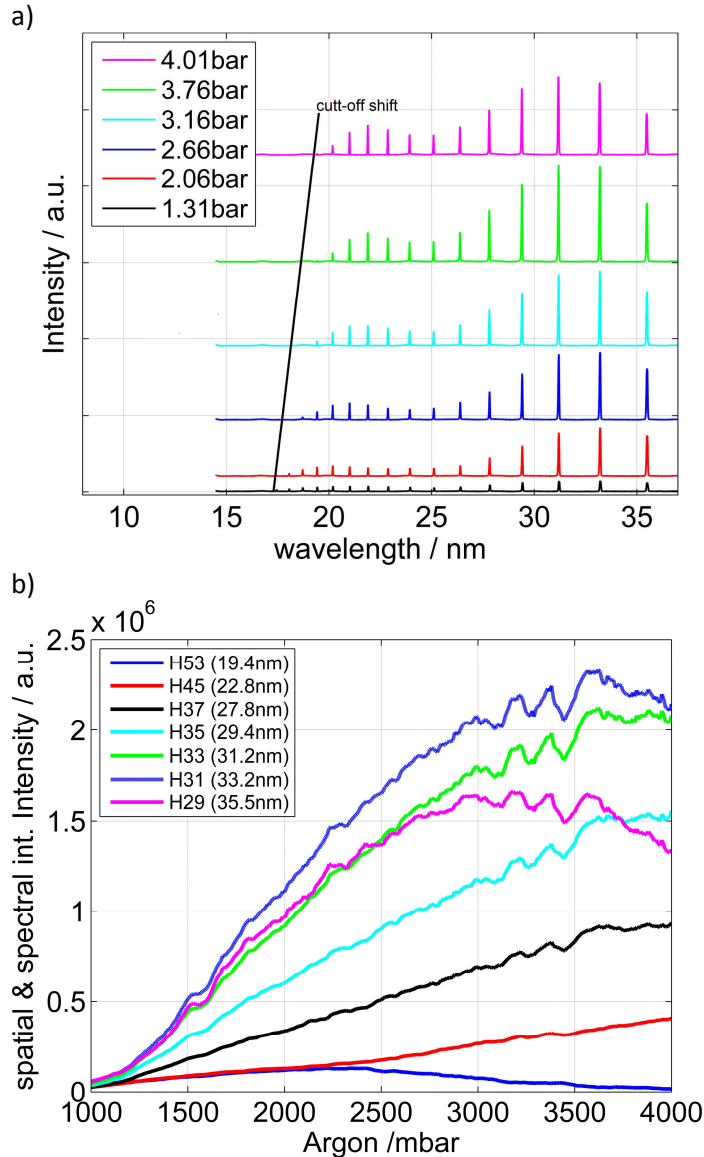
Figure 23: The Target: 4x 50µm argon jets. Scanning range: from 1 to 4 bar Argon backing pressure. Focus: focus plane before target in z-direction. The pulse energy was 400 µJ and the pulse duration 570 fs. a) Qualitative overview of the spectral shape development of an argon pressure scan. Pulse energy shifts and pulse broadening decreased the intensity within the course of the measurement and led to cut-off shifts. After the measurement the pulse energy is 375 µJ and the pulse duration 870 fs. b) Plot of the spectrally integrated harmonic yield against the pressure. (scan51)

(focus before target) have to be compared to Figure 22a (focus in target) and visualize the development of the spectral shape, related to the argon backing pressure. In Figure 23a and Figure 24a, where the focus position was in front of the target, the cut-off was extended and high harmonics could be observed up to the aluminum absorption edge at $17\,nm$ in Figure 24a. The generation of these additional harmonics was caused by optimization of the phase matching conditions.

Furthermore, the harmonics were sensitive for pressure induced phase matching, because the ionization level was reduced. The saturation mechanism - induced by free electrons- could not be observed anymore at the low order harmonics of the spectrum, because the free electron density was decreased. However, the focus position in front of the target decreased the maximal harmonic yield by 25% - cf. Figure 22b. Reference [37] shows that the defocusing induced by free electrons can improve the conversion efficiency, when the laser focus is located after a single gas jet. If this principle applies for a multi-jet target or not has to be investigated in future.

5.2.4   Laser induced intensity shifts

In addition to the fast pulse fluctuations discussed in Section 5.2.1, slow drifts in energy and time occurred in addition. In the Figure 23a a drift in pulse energy and pulse broadening of the driver pulse can be observed in the spectrum. The cut-off shifted to longer wavelengths within the pressure scan. The shift could be detected at pressures $p > 2\,bar$. In this case the change of the cut-off is not connected to the pressure induced phase-shift or at least not exclusively, because the intensity drifted at the same time. Pulse energy shifted from $400\,\mu J$ to $375\mu J$ and the pulse duration from 570 to $870\,fs$.

In order to sort results, where changes in intensity occurred within a pressure scan, the pulse energy and pulse duration of the driver laser have been always determined before and after a pressure scan. In the results presented in Figure 23 both pulse energy and pulse duration shifted and lead to lower peak intensities. However, the long term energy drifts were relatively stable within the beam time. Corrections were made only in the warm-up phase of the system by adjusting the power of the pump diodes of the main amplifier. The pulse broadening caused more problems, because it was occurring all the time. Therefore the scan duration of the scans was limited to ~15 min, in order to minimize the pulse broadening influence. Anyway, a lot of data series had to be excluded, because the pulse duration was extended by a factor of two within the 15 min. The exact origin of the pulse broadening could not be identified. The compression of the pulse was affected, because compressor adjustments reestablished the pulse duration of $580\,fs$. Additionally, satellites in the time structure were observed, which were induced by soliton wavelength shifts in the seed system. By readjusting the center wavelength to $1030\,nm$, the satellites were suppressed.

The observed intensity changes, introduced by the pulse broadening in the order of a factor of two, should be clearly influencing the cut-off. Interestingly, not all the intensity changes led to changes in the observed spectrum. This indicates that the cut-off shifted beyond the aluminum absorption edge. Since the detection of cut-off changes was suppressed by the aluminum filter (detection below 17 was not possible, because of the aluminium edge), the real peak intensity must be significant larger than the approximated intensity of $2.33 \cdot 10^{14} W/cm^2$. Considering the relative change by a factor of two due to pulse broadening, as well as the $17\ nm$ aluminum edge as reference, an intensity of at least $3.8 \cdot 10^{14} W/cm^2$ would be needed to generate a cut-off wavelength, which shifts beyond the aluminum absorption edge.
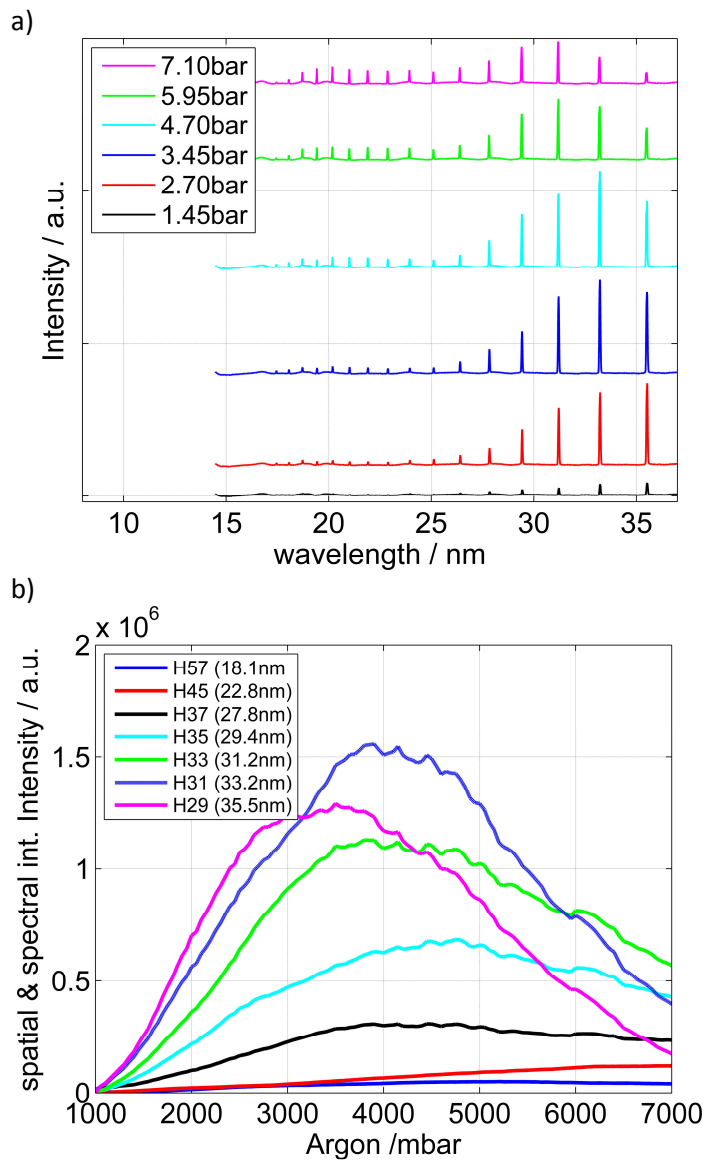
a)

b)

Figure 24: The Target: 4x 50µm argon jets. Scanning range: from 1 to 7 bar Argon backing pressure. Focus: focus plane before target in z-direction. The pulse energy was 400 µJ and the pulse duration 570 fs. a) Qualitative overview of the spectral shape development of an argon pressure scan. b) Plot of the spectrally integrated harmonic yield against the pressure. (scan49)

The aluminum filter was replaced by a zirconium filter, in order to record a spectrum above the aluminum absorption edge (see Figure 20).

However, immediately the high peak intensity damaged the filter, because zirconium has a smaller damage threshold than aluminum. Usually the distance between target and filter has to be expanded to lower the peak intensity. Due to divergence the beam expands spatially while propagation. However, the chamber dimensions were fixed in this setup and therefore the spectrum was restricted to the aluminum filter.

Figure 24 shows an argon scan up to $7\ bar$ without observed long term intensity shifts. The observed spectrum stayed constant over the complete course.

5.2.5 Determination of the roll-over pressure

This section illustrates an example for the determination of the roll-over pressure through. In order to optimize the generation of high-order harmonics in the observed spectrum, the focus was located before the target. In Figure 25 the results for selected harmonics are shown. The harmonic yield increases for all wavelengths with rising pressure. The $22.80\ nm$ (cyan) and $23.89\ nm$ (green) curves do not feature a distinct maximum, but they exhibit a stepwise increase of the signal. It is assumed that the steps in the plot indicate the pressure $p_{\pi,\lambda}$ corresponding to a phase shift of π. This behavior can be drawn back onto the blurring effects induced by the 3-D and time domain nature of a laser pulse – cf. Chapter 5.1.

The $26.37\ nm$ (red) curve shows as well a step, which is more distinct than $22.80\ nm$ (cyan) and $23.89\ nm$ (green). In this selection only the $27.80\ nm$ curve (blue) shows a distinct peak. Since, the backing pressure range was limited to $7\ bar$, a phase oscillation could not be verified. As well absorption could be the dominating effect for the roll-over in the measured signal. Also a superposition of both effects is possible. Since, the actual pressure in the interaction zone is unknown, but both absorption and dispersion are related to the pressure, approximations cannot be done. Nevertheless, the transmission characteristic of argon in the wavelength range indicates absorptions effects – cf. Figure 11. If this is the case, no significant QPM-enhancement can be expected in the wavelength range larger than $28\ nm$.
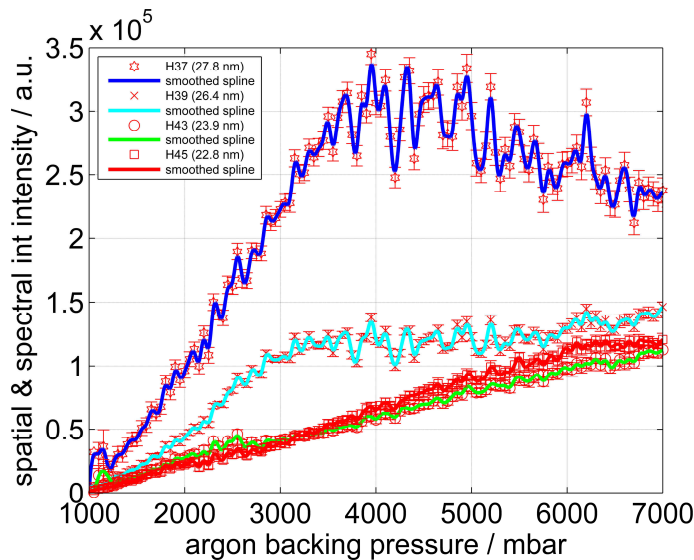
Figure 25: Spatial and spectrally integrated harmonic yield plotted as function of the backing pressure for selected harmonics. The pulse energy was 400 μJ and the pulse duration 570 fs. The plot gives information about the specific roll-over pressure, which corresponds to a phase-shift of π and is needed to accomplish QPM. Furthermore, wavelength related absorption can be obtained.

Table 1: Determined roll-over backing pressures from Figure 21 and Figure 24b

Harmonic No.	Wavelength / nm	Roll-over backing pressure $p_{\pi,\lambda}$ /mbar		Limitation
57	18,1	<1600	/step	phase / absorption
55	18,7	<1600	/step	phase / absorption
53	19,4	<1600	/step	phase
51	20,2	<1600	/step	phase
49	21,0	1200±300	/step	phase
47	21,9	1800±300	/step	phase
45	22,8	2000±300	/step	phase
43	23,9	2400±300	/step	phase
41	25,1	2600±300	/step	phase
39	26,4	3200±300	/step	phase
37	27,8	3900±300	/peak	phase / absorption
35	29,4	4600±200	/peak	phase / absorption
33	31,2	3700±200	/peak	phase / absorption
31	33,2	4000±200	/peak	absorption
29	35,5	3200±200	/peak	absorption

In Table 1 the determined roll-over backing pressures and the indication characteristic (peak/step) for the observed harmonics are listed and obtained from the data shown in Figure 24 and Figure 25. Furthermore, the supposed dominating effect, which limited the signal increase, is labeled in the last column of the table (phase / absorption).

The harmonics 29 to 39 feature distinct peaks as a roll-over. The pressure scanning range was limited to $7\,bar$ and therefore it was not possible to exclude absorption as roll-over mechanism for the harmonics 33 to 37. The harmonics 39 to 49 are showing a stepped signal trend. The first observed step in these scan was interpreted as correspondent π phase shift.

The harmonics 51 to 57 have a stepped signal increase at higher pressures, which corresponds to a multiple of a π phase shift. In this case it seems to be that the π phase shift was below a pressure of $1.6\,bar$. In fact, at this pressure level the signal-to-noise ratio was too low in order to extract reasonable data.

As mentioned, the steps have been interpreted as phase-mechanism and the correspondent pressures have been chosen as starting pressures for the QPM hydrogen scans.

5.3   QPM - Hydrogen pressure scans

Hydrogen is more difficult to pump than argon. To support the turbo-pump a roots-pump was attached to the chamber. However, the noise and the vibrations of this pump affected other experiments in the room. For this reason this pump could only be used sporadically. Most of the experiments were performed only with the turbo-pump. In order to protect it against an overload,

the hydrogen pressure was limited to 1 bar backing pressure. The spinning frequency has been decreased significantly at larger pressures. Furthermore, the background pressure in the chamber raised into the pressure range of the low $10^{-1}mbar$. Backing pressure of 2 bar could be maintained with the additional roots-pump. The results for the 1 and 2 bar scans are presented and discussed separately in the following sections.

5.3.1 Hydrogen pressure scans till 1 bar

The exemplary roll-over argon backing pressures data presented in Table 1 provided the initial conditions for the QPM hydrogen pressure scans, in order to find the optimal pressure argon and hydrogen conditions for maximal enhancement of the harmonic yield. In these measurements the argon backing pressures were kept constant, while the hydrogen pressure was raised stepwise.
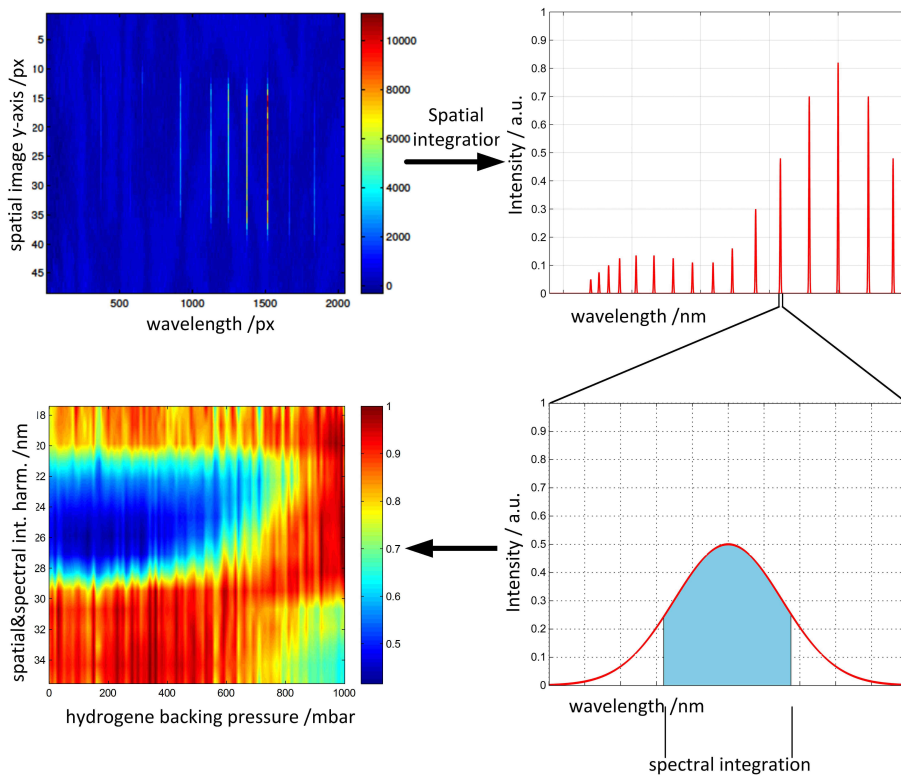
Figure 26: Schematic description of the data analysis and data representation. 1. Spatial integration (y-direction) of the spectrum for each pressure increment. 2. Applying a Gaussian fit on each harmonic to determine signal and background, followed by a spectral integration over the FWHM width of the fitted curve. 3. Combining the analyzed data in a color plot for clear representation, where the spectral integrated signal is plotted against the pressure. Note that by adding only the spatial and spectral integrated data to the plot, the characteristic spectral distribution (comb structure) and especially the gaps in a HHG spectrum are suppressed. Although this could give an impression of a continuum, it clarifies the information message.

The desired information is obtained by relating the detected signal trace to a reference signal, which was recorded in the absence of hydrogen. Therefore, the measurements were always started at $0\,bar$, so that the reference signal was taken at the same conditions (alignment, intensity).

The basis of the applied data analysis of the hydrogen scans is identical to the argon scans – see Figure 26. In a successive operation, first the spectrum has been integrated spatially. Then each single harmonic has been fitted to a Gaussian function to determine the background and width, in order to apply a spectral integration (FWHM).

The background corrected and both spatial and spectral integrated intensity in arbitrary units (FWHM) of each harmonic is plotted against the hydrogen pressure. To give an overview of the influence of the hydrogen on the signal over the complete measured spectrum, the data is presented in two different color plots. By adding only the spatial and spectral integrated data to the plot, the characteristic spectral distribution (comb structure) and especially the gaps in a HHG spectrum are suppressed. Although this could give an impression of a continuum, it clarifies the information message.

Figure 27 to Figure 30 are showing the results of hydrogen pressure scans for four different argon backing pressures from $2.4\,bar$ to $4.8\,bar$. The pressure range has been chosen in order to observe signal enhancement in the high-order harmonics ($18\,nm - 25\,nm$). The figures show the relative intensities related to the hydrogen pressure. To maintain the large peak difference of low and high harmonics in the color plot, each harmonic as function of the pressure is normalized to the maximal harmonic yield. In the Figure 27b to Figure 30b the relative change (enhancement) as function of the hydrogen pressure is shown in a color plot.

In all exhibited scans (Figure 27 to Figure 30) the fluctuations are visible (striped pattern), which are induced by the oscillating pump diode temperature and discussed in the previous chapter.

All scans are showing a hydrogen induced enhancement of the harmonic yield related to the given argon backing pressure. The enhancement started to evolve with increasing hydrogen backing pressure at approximately $600\,mbar$. As expected from the simulations (Chapter 3.2), the enhancement behavior is distinctly varied for different argon backing pressures regarding to the magnitude of enhancement and wavelength range (wavelength selective). Only a small wavelength range can be enhanced by the QPM mechanisms at the same time.

a)

b)

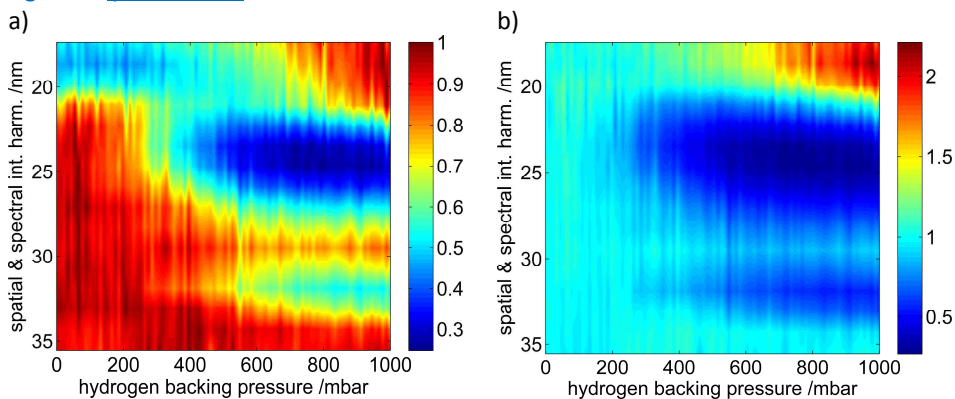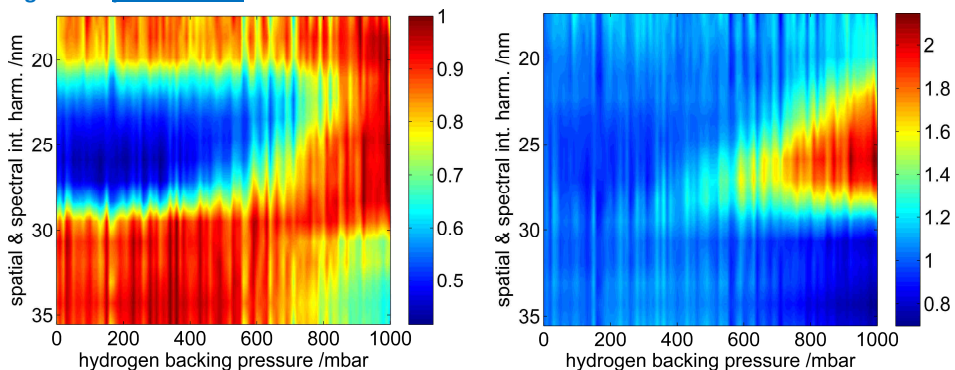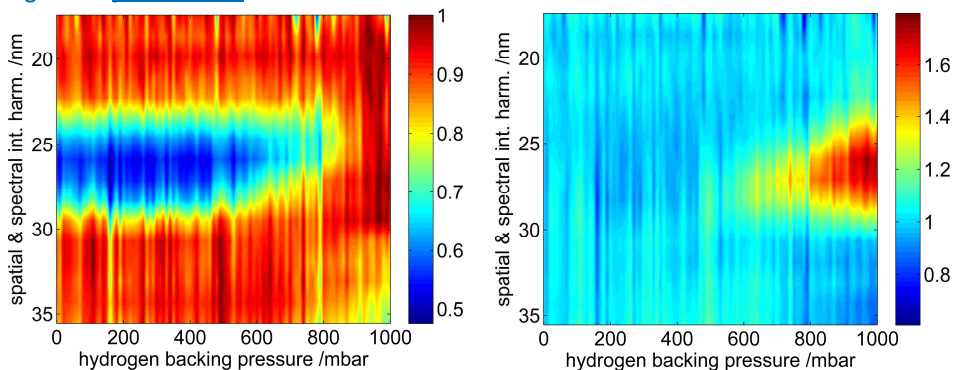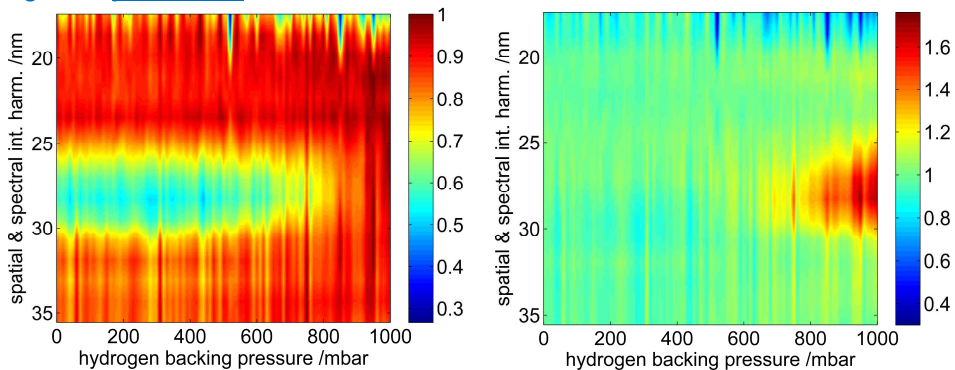**Spatially and spectrally integrated harmonics as function of hydrogen backing pressure at an argon backing pressure of p=2400,3200, 4000 4800 mbar. Focus plane before target to optimize the high-order harmonics. The pulse energy was 400 µJ and the pulse duration 570 fs. (a) Relative intensity evolution separately normalized to the maximum signal for each harmonic. (b) Displays the relative change (enhancement) of the harmonic yield compared to hydrogen pressure p=0mbar. Note that by adding only the spatial and spectral integrated data to the plot, the characteristic spectral distribution (comb structure) and especially the gaps in a HHG spectrum are suppressed. Although this could give an impression of a continuum, it clarifies the information message.**

In Figure 31 the enhancement profiles for several argon pressures at 1 bar hydrogen backing pressure are shown for comparison. They show wavelength selective phase matching behavior of the target. The first rising slope of every curve decreases with growing argon pressure and shift slightly to higher wavelength. The strongly rising absorption cross-section beginning at $\sim 27\,nm$ suppresses the distinct enhancement peak at higher argon backing pressures.

The maximal achieved enhancement factor was 2.2 ± 0.2. The uncertainty was obtained from the error propagation of the determined uncertainty of the data analysis. With increasing argon pressure this value decreased, because of the pressure and wavelength related absorption. Nevertheless, this value deviates by a factor of 8 compared to the theoretical maximum of a factor of 16 for a 4-jet target.

No hydrogen induced roll-over is visible in any of the displayed scans. It can be expected that the enhancement could be increased by applying larger hydrogen pressures, in order to optimize the phase relation in the matching-zones of the target. This consideration is important for the evaluation of the following approximation.

To approximate the theoretical QPM-enhancement considering the experimental argon pressure curves from Figure 25, the quadratic growth increase of the harmonic yield between 1 bar and $p_{\pi,\lambda}$ (Table 1) were fitted. For larger pressures the ideal quadratic increase of QPM was interpolated. The interpolation indicates the maximal possible enhancement obtained by QPM as a function of the argon backing pressure. For four selected wavelengths both fit and interpolation at higher pressures are shown in Figure 32. In the main Figure 32 clarifies that the achieved results agree with the interpolation in the probed argon pressure range . In Figure 32a-b the argon backing pressure limits the enhancement. In order to achieve maximal enhancement the pressure requires to be $p = N_{QPM} \cdot p_{\pi,\lambda}$.
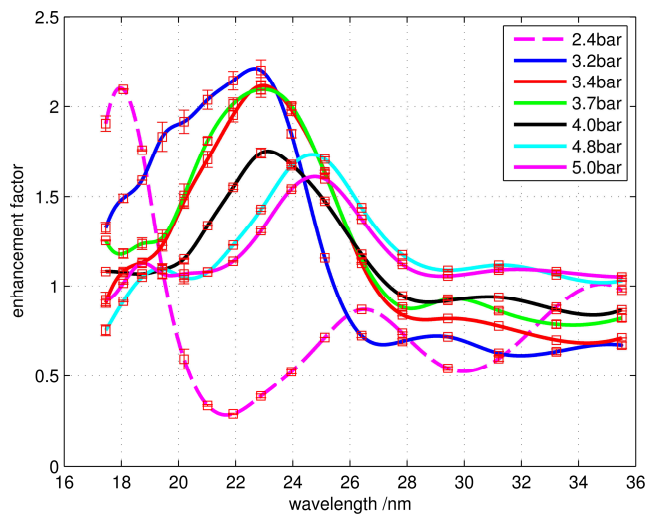
Figure 31: Spectrally resolved QPM enhancement profiles for different argon backing pressures at 1 bar hydrogen. The spectrally limited enhancement shifts to higher wavelength with increasing argon pressure. The strongly rising absorption cross-section begins to decrease the relative enhancement at ~27 nm.
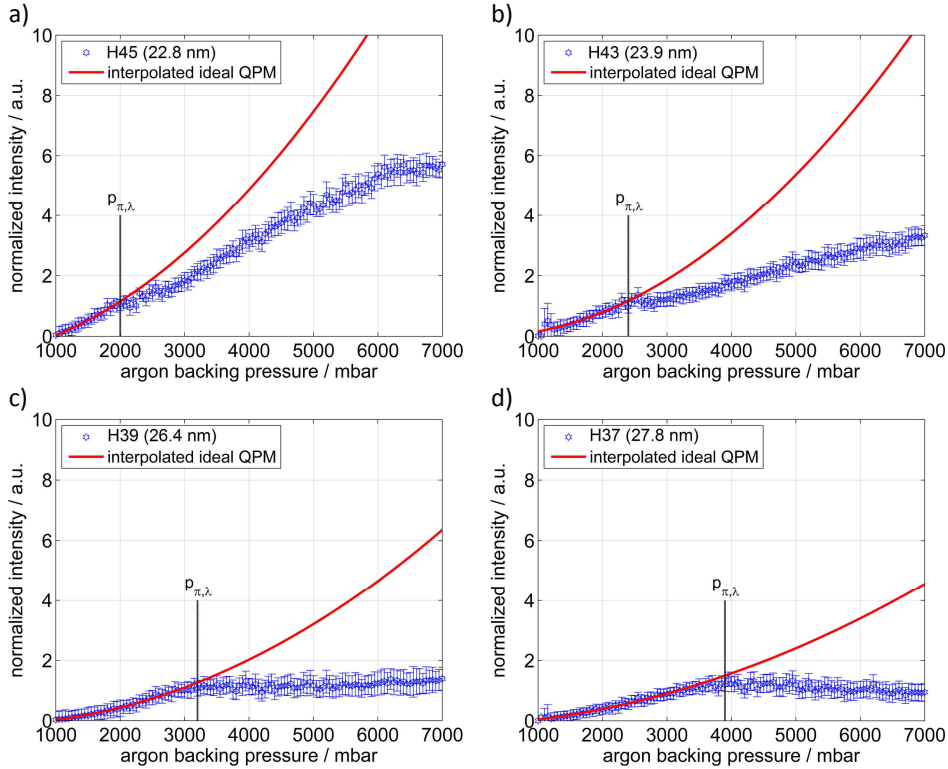
Figure 32: Interpolation of the ideal growth of the harmonic yield for QPM. Harmonic yield fitted to the data in the range between 1bar to $p_{\pi,\lambda}$, because a quadratic increase can be assumed, and interpolated for higher pressures. The interpolation indicates the optimal signal growth.

In Figure 32c-d deviations between the interpolation and the experimental enhancement at higher pressures are visible. The maximal enhancement at the given argon backing pressure could not be gained, because either the phase-mismatch was not corrected sufficiently (hydrogen pressure was limited), or self-absorption in the interaction zone and/or in the residual gas in the chamber occurred. The results of the simulations show a strong relation between the hydrogen pressure and the enhanced wavelength – see Figure 16.

According to the simulation, the phase matching for high-order harmonics occurs at lower hydrogen pressures than for low order harmonics. The experimental results (Figure 27 to Figure 30) show an ambiguous behavior compared to the simulated results, but indicate rather a contrary behavior. In the results the low order harmonic yield increases at lower pressures.

This behavior is theoretical possible, when negative values for Δk (Eq.2.33) are obtained due to large ionization rate and Gouy-shift influence. This would invert the observed wavelength relation in the simulation – cf. Figure 16. However, in that case the observed mechanism of the argon shift cannot be explained anymore, because it must be inverted as well, and the peak shift with growing pressure to lower wavelength – cf. Figure 31. Certainly the nature of 1-d simulation expresses only a simplified picture of complex HHG-process. For this reason a good agreement in all aspects cannot be expected.

5.3.2 Hydrogen pressure scans till 2 bar

During the experiment the roots-pump was only used a few times. In those cases the pump efficiency of the complete vacuum system was increased and allowed to improve the background pressure in the experimental chamber (residual gas) by one order of magnitude to the low $10^{-2}\,mbar$ range. Furthermore, hydrogen backing pressures of $2\,bar$ could be performed.

Compared to the exhibited hydrogen scans up to $1\,bar$ in Section 5.3.1, these scans were carried out in changed focus geometry. In order to expand the Rayleigh length, a lens with a focal length of $f = 1000\,mm$ was inserted $300\,mm$ before the focus lens. The modified Rayleigh length decreased the phase-mismatch induced by the Gouy-shift and intensity variation within the target. At the same time the peak intensity was reduced by approximately $30\,\%$, because the focus was expanded as well.

In this configuration the focus could be centered on the target without the observation of the plasma lines – cf. Figure 21. When the focus was positioned before the target, the high order harmonics of the observed spectral range were optimized. Harmonics were still observable up to the aluminum edge. In a pure hydrogen pressure scan up to $2\,bar$ backing pressure, no harmonics could be observed. This fundamental requirement for QPM was after the change of geometry still fulfilled.

In Figure 34 and Figure 33 QPM hydrogen scans up to $2\,bar$ hydrogen backing pressure are presented for $7\,bar$ and $9.5\,bar$ argon backing pressure respectively. The pressure of $9.5\,bar$ was achieved by bypassing the argon pressure controller. In these measurements the focus was centered on the target. The detected cut-off wavelength was at $22.8\,nm$ and this is the reason for the smaller spectral range in the scale of the color plots (24 to 35 nm) compared to the results in Section 5.3.1.

In both scans a maximal enhancement of the harmonic yield by a factor of 3.1 ± 0.4 was observed, at hydrogen backing pressures higher than $1.5\,bar$. In the $7\,bar$ argon backing pressure scan an improvement of the harmonic yield in the spectral range around $24\,nm$ and between $28\,nm\,to\,35\,nm$ was observed for the first time in the experiment. This indicates that the roots-pump improved the vacuum conditions in the experimental chamber and minimized absorption effects. However, at the $9.5\,bar$ argon backing pressure scan, this enhancement between $28\,nm\,to\,35\,nm$ could not be observed anymore. Whether the absence of the enhancement was induced either by absorption or by phase matching effects cannot be distinguished, because it was not possible to accomplish a reliable argon pressure scan up to $9.5\,bar$, because the pressure above $7\,bar$ could not be controlled.

In these measurements it is noticeable that, in contrast to the measurements in Section 5.3.1, the wavelength related enhancement increased with rising
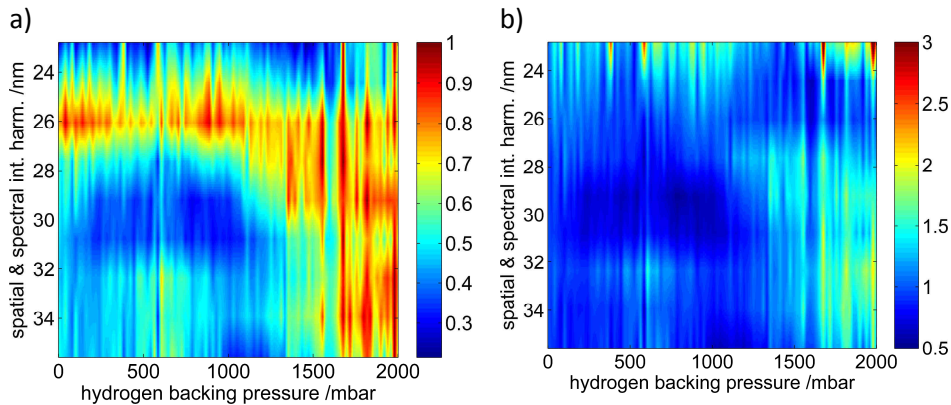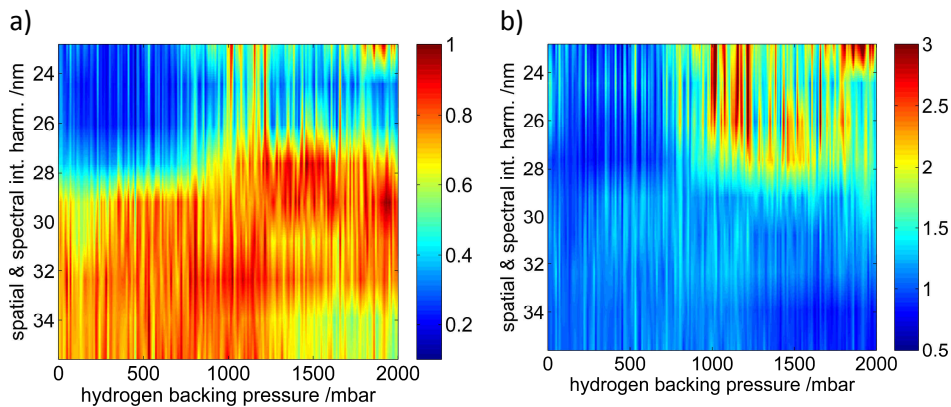
a) b)

Figure 33: p=9500 mbar

a) b)

Figure 34: Spatially and spectrally integrated harmonics plotted against hydrogen backing pressure at an argon backing pressure of p=7000 mbar. Focus centered on target. (a) Relative intensity evolution separately normalized to the maximum signal for each harmonic. (b) Displays the relative change (enhancement) of the harmonic yield compared to hydrogen pressure p=0mbar. . Note that by adding only the spatial and spectral integrated data to the plot, the characteristic spectral distribution (comb structure) and especially the gaps in a HHG spectrum are suppressed. Although this could give an impression of a continuum, it clarifies the information message.

hydrogen pressure first at the short wavelength. This behavior correlates with the results of the simulation in Figure 16.

Admittedly, the exact reason for the change of this behavior is unknown. A direct comparison between the results presented in Section 5.3.1 and in this section is actually not possible, because too many parameters changed at the same time. It was not possible to collect enough meaningful data in this focus geometry in order to complete the behavior pattern.

Already the change of the focus position probably caused this behavior. In Figure 35a-d hydrogen scans at $5\,bar$ argon backing pressure for four selected harmonics are shown. The scans were performed at three different focus positions. The position $z = 0\,\mu m$ corresponds to the beginning target and $z = 260\,\mu m$ to the target center. Only low order harmonics visible at each focus positions were compared. It is clearly visible that, for the compared harmonics, the focus position had a stronger influence on the harmonic yield than varying
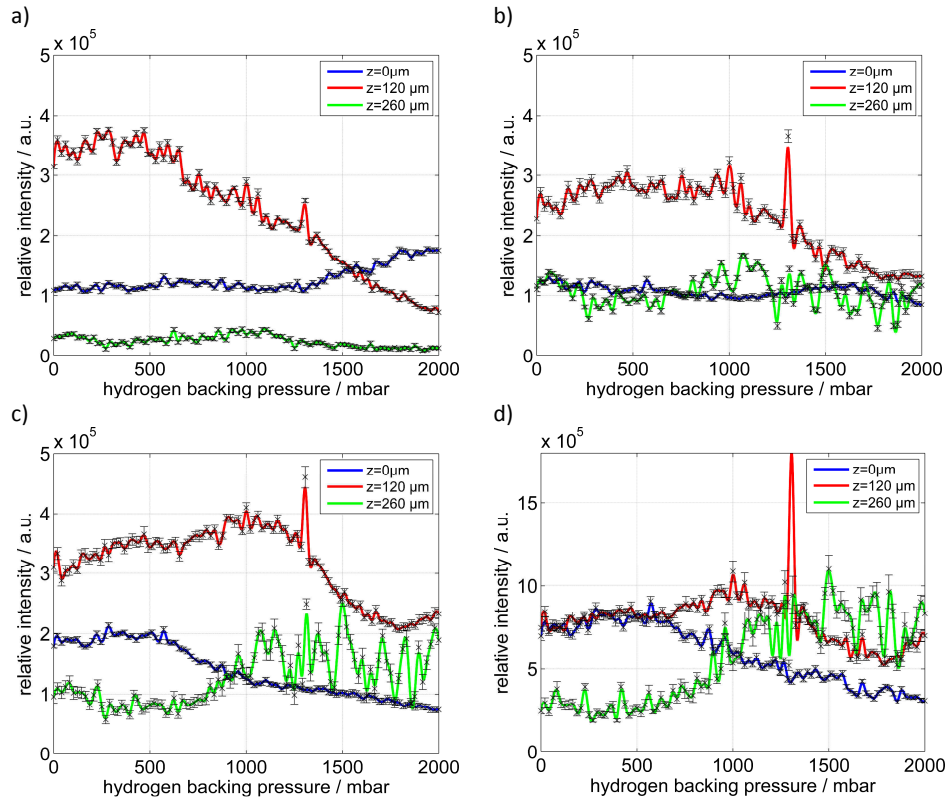
Figure 35: Influence of the focus position z on the harmonic yield for selected harmonics (a) H45 -22.8 nm, (b) H41 - 25.1 nm, (c) H37 - 27.8 nm, (d) H33 - 31.2 nm within a hydrogen scan at 5 bar argon backing pressure. The focus position tremendously modified the level and the course of the harmonic yield within the hydrogen scans.

the hydrogen pressure. At $z = 120\ \mu m$ the starting level of harmonic yield (red) was by a factor between 2 and 3 higher than the harmonic yield in the other focus positions –see Figure 35a-c. Furthermore, the harmonic yield could only be extended by maximum 30%, considering that the peak between $1.2\ bar$ and $1.4\ bar$ backing pressure is an outliner.

In the other focus positions in Figure 35a-c maximal enhancement factors of 2 could be observed. However, the absolute signal was still smaller by a factor of 2 than at the position $z = 120\ \mu m$. Only in (d) a hydrogen induced signal gain was observed at the position $z = 260\ \mu m$, which reached the maximal level of the one at focus position $z = 160\ \mu m$. The overall picture given by the Figure 35 indicates that the influence of the focus position is too strong.

6 Conclusion

There is an increasing scientific interest in improving the pulse parameters, (pulse shape and spectral characteristics), of free-electron lasers (FEL). A promising approach is to seed the FEL with a laser-based table-top XUV-source using high harmonic generation (HHG). It is planned to implement an external laser based XUV-seeding source into the „Freie-Elektronen Laser Hamburg II" at the „Deutsche-Elektronensynchrotron" in Hamburg. In order to generate the needed seed energy of $1\,nJ$ in a variable spectral range from $10\,nm$ to $40\,nm$ (XUV - extreme ultraviolet) at $100\,kHz$ repetition rate, a new modular multi-nozzle XUV-source has been developed. In this work the new HHG source was tested at high repetition rates.

This HHG target consists of several gas jets in an open space geometry, which allows high average powers without damage threshold. The multi-jet source allows high harmonic generation in an inert gas by successive coherent super-position. In order to obtain coherent superposition, the phase between the fundamental beam and the generated harmonics has to be adjusted between each single jet. The concept of quasi-phase matching (QPM) is realized with alternating HHG-jets and hydrogen jets, where the hydrogen acts as a phase matching medium to correct the phase occurred in the HHG-jet. Hydrogen is completely ionized at driver intensities $\geq 3 \cdot 10^{14}\,W/cm^2$ and therefore cannot contribute to the HHG-process. Furthermore, the 1d theory predicts a quadratic signal increase.

The phase relationship between the fundamental beam and high harmonics can be controlled by pressure tuning of the individual gases, in order to achieve coherent superposition of harmonics generated in the multi-jet target. By measuring the change in the harmonic yield by applying hydrogen pressure scans (0 to maximal 2 bar) at various argon pressures, the optimal pressure combination can be determined.

The functional principle of the presented HHG QPM dual-gas target was already successfully tested in proof of principle experiments in advance to the present work. Within the scope of this thesis, a dual-gas target was characterized for the first time at a repetition rate of $75\,kHz$ with the driver laser wavelength of $1030\,nm$. In the QPM experiments, a maximal enhancement factor of 2.2 ± 0.2 in the $0\,to\,1\,bar$ hydrogen courses and 3.1 ± 0.4 in the $0\,to\,2\,bar$ hydrogen scans was observed for the harmonics H29 to H57. These results deviated from the 1d theory and can be explained by the 3D effects such as temporal and spatial properties of a gaussian beam, and inhomogeneous gas density in the jet. To approximate a realistic QPM-enhancement limit for a given target, one has to interpolate the quadratic increase of the harmonic yield beyond the roll-over pressure (corresponds to a phase-mismatch of π) in a pure argon scan – see Figure 32. Up to the roll-over pressure, signal growth is

quadratic. Attention should be paid to the fact that the determined factors describe relative enhancement with respect to the given argon backing pressure.

An absolute enhancement was not determined in this work. The absolute harmonic yield at $7\,bar$ argon backing pressure was larger than any result using the QPM approach at lower argon pressures. On the contrary no QPM-effect could be observed at $7\,bar$ with respect to the measurements without additional gas pump power. This indicates that the background pressure in the experimental chamber induced self-absorption.

In former studies, the QPM-target demonstrated the largest signal gain in the cut-off regime. However, the characterization of a possible QPM induced cut-off extension was not possible for the given experimental conditions. The detection of harmonics >H57 was limited by the aluminum absorption edge ($17\,nm$). Alternative filter material such as zirconium, which allows to observe >H57, could not be used, because the damage threshold was too low. This fact prevented the measurement at the cut-off range of the generated spectrum.

In general, the experimental conditions were challenging in different aspects. First, the first the present laser parameters with a driver pulse energy of $400\,\mu J$ and the requirement of intensities $I > 3 \cdot 10^{14} W/cm^2$ made it necessary to choose a hard focusing geometry, with a focal length $f = 75\,mm$, resulting in a Rayleigh length of $(400 \pm 50)\,\mu m$. Thus, the intensity varied by a factor of 2 within the target. Since the 4-QPM-period target had an overall length of $470\,\mu m$, the phase matching conditions were not the same for all jets. Usually focal lengths $f > 500\,mm$ should be used in future in order to achieve Rayleigh lengths 5 to 10 times larger than the target. This would homogenize the intensity in the target and also reduce the Gouy-shift influence.

Second, using the chosen focus geometry, the alignment and reproducibility of the experimental conditions were difficult to maintain. Additionally it has to be mentioned that the focus position tremendously modified the level and the profile of the harmonic yield within the hydrogen scans. This behavior is caused by the focus geometry and can be an additional reason for the deviation to the 1d theoretical enhancement.

Third, the stability of the laser turned out to be insufficient for stable QPM HHG, because both the short and long time laser power stabilities were not fulfilled. The pressure controlled phase-shift was affected by the intensity induced ionization rate. Since the phase-mismatch is a function of both pressure and ionization rate, the changes in the harmonic signal cannot be related either to the former or the latter, exclusively. The measured harmonic yield fluctuated by approximately 20% in the pure argon scans. As expected, the fluctuation in amplitude of the harmonic yield was one order of magnitude larger in the QPM scans. In spite of all the difficult conditions an obvious signal increase

was detected. A QPM-effect was observed in the pressure range in the scans, where the fluctuation amplitude of the enhancement was particularly large.

In addition to the experiment a simulation was performed. In general, the qualitative results of the simulation were confirmed by the experimental results. In the simulation it was obtained that the spectral range, in which enhancement takes place, could be selected by choosing suitable combination of argon and hydrogen pressures. This behavior was observed in the results of the experiments.

In order to achieve larger enhancement factors, higher backing pressures would be needed according to the interpolation of the observed data. Nevertheless, higher pressures could also lead to distortion of the laser by plasma defocusing or to self-absorption of the harmonics. To avoid problem of increased pressure, improvements can be made to the technical design relating to gas flow within the target. At the current design the "parker valves" are bottleneck and limit the flow in the target.

In this work $500\,fs$ pulses were used. In future the use of sub-10fs pulses will be more sensitive to the focus geometry and dispersive effects. In this case a technical improvement such as the individual control of each HHG-jet and phase matching jet should be carried out, in order to achieve ideal phase matching conditions over the complete target.

In summary, it was possible to observe relative enhancement at high repetition rates with the dual-gas target. However, in future experiments it is recommended to use a stable laser with higher peak powers. Furthermore, the technical design of the target has to be improved in several aspects, especially the gas flow within the target and individual pressure control of each nozzle. This optimization will reduce the backing pressures to a lower level and more QPM-periods will be feasible. In addition, the gas pump efficiency has to be improved in order to reduce the background pressure in the experimental chamber. The implementation of a differential pump stage could facilitate the necessary improvement. These improvements may allow an improved HHG-efficiency needed to seed FLASH II.

Amendment:

So far it was assumed that hydrogen needs to be fully ionized in order to be a passive phase matching medium. It was considered that this occurs at driver laser intensities $I > 3 \cdot 10^{14} W/cm^2$. Furthermore, it was assumed that hydrogen is easier to ionize than noble gases, because of the lower ionization potential. The physical background of the phase matching ability of hydrogen was recently investigated in detail by Wang et. al. [53]. In their research they

claimed that hydrogen ionizes with the same probability as argon at intensities $I > 3 \cdot 10^{14} W/cm^2$. However, the recombination cross section of hydrogen is one order of magnitude smaller compared to argon, at the same driver intensity. Since the harmonic yield is closely related to the recombination cross-section [54], the expected harmonic yield would be one order of magnitude lower than argon. Thereby, the destructive interference due to hydrogen harmonics can be neglected. For this reason hydrogen fulfills the requirements as phase matching medium under the experimental conditions used in this thesis.

References

1.   A. McPherson, G. Gibson, H. Jara, U. Johann, T. S. Luk, I. A. McIntyre, K. Boyer, and C. K. Rhodes, "Studies of multiphoton production of vacuum-ultraviolet radiation in the rare gases," J. Opt. Soc. Am. B **4**, 595–601 (1987).

2.   X. F. Li, A. L'Huillier, M. Ferray, L. A. Lompré, and G. Mainfray, "Multiple-harmonic generation in rare gases at high laser intensity," Phys. Rev. A **39**, 5751–5761 (1989).

3.   U. Teubner and P. Gibbon, "High-order harmonics from laser-irradiated plasma surfaces," Rev. Mod. Phys. **81**, 445–479 (2009).

4.   P. B. Corkum, "Plasma perspective on strong field multiphoton ionization," Phys. Rev. Lett. **71**, 1994–1997 (1993).

5.   M. Lewenstein, P. Balcou, M. Y. Ivanov, A. L'Huillier, and P. B. Corkum, "Theory of high-harmonic generation by low-frequency laser fields," Phys. Rev. A **49**, 2117–2132 (1994).

6.   E. L. Falcão-Filho, C.-J. Lai, K.-H. Hong, V.-M. Gkortsas, S.-W. Huang, L.-J. Chen, and F. X. Kärtner, "Scaling of high-order harmonic efficiencies with visible wavelength drivers: A route to efficient extreme ultraviolet sources," Applied Physics Letters **97**, 061107 (2010).

7.   L. Z. Liu, K. O'Keeffe, and S. M. Hooker, "Optical rotation quasi-phase-matching for circularly polarized high harmonic generation," Opt. Lett. **37**, 2415–2417 (2012).

8.   C. Spielmann, C. Kan, N. Burnett, T. Brabec, M. Geissler, A. Scrinzi, M. Schnurer, and F. Krausz, "Near-keV coherent X-ray generation with sub-10-fs lasers," Selected Topics in Quantum Electronics, IEEE Journal of **4**, 249–265 (1998).

9.   F. Krausz and M. Ivanov, "Attosecond physics," Rev. Mod. Phys. **81**, 163–234 (2009).

10.   X. Zhang, A. L. Lytle, T. Popmintchev, X. Zhou, H. C. Kapteyn, M. M. Murnane, and O. Cohen, "Quasi-phase-matching and quantum-path control of high-harmonic generation using counterpropagating light," Nature Physics **3**, 270–275 (2007).

11.   B. Dromey, M. Zepf, M. Landreman, and S. M. Hooker, "Quasi-phasematching of harmonic generation via multimode beating in waveguides," Opt. Express **15**, 7894–7900 (2007).

12.   I. Christov, H. Kapteyn, and M. Murnane, "Quasi-phase matching of high-harmonics and attosecond pulses in modulated waveguides," Opt. Express **7**, 362–367 (2000).

13.   A. H. Sheinfux, Z. Henis, M. Levin, and A. Zigler, "Plasma structures for quasiphase matched high harmonic generation," Applied Physics Letters **98**, 141110–141110–3 (2011).

14.   J. Seres, V. S. Yakovlev, E. Seres, C. Streli, P. Wobrauschek, C. Spielmann, and F. Krausz, "Coherent superposition of laser-driven soft-X-ray harmonics from successive sources," Nature Physics **3**, 878–883 (2007).

15.   A. Pirri, C. Corsi, and M. Bellini, "Enhancing the yield of high-order harmonics with an array of gas jets," Phys. Rev. A **78**, 011801 (2008).

16.   A. Willner, "A High Repitition Rate XUV Seeding Source for FLASH2," Dissertation, Universität Hamburg (2011).

17.   A. Willner, F. Tavella, M. Yeung, T. Dzelzainis, C. Kamperidis, M. Bakarezos, D. Adams, R. Riedel, M. Schulz, M. C. Hoffmann, W. Hu, J. Rossbach, M. Drescher, V. S. Yakovlev, N. A. Papadogiannis, M. Tatarakis, B. Dromey, and M. Zepf, "Efficient control of quantum paths via dual-gas high harmonic generation," New Journal of Physics **13**, 113001 (2011).

18.   B. Faatz, N. Baboi, V. Ayvazyan, V. Balandin, W. Decking, S. Duesterer, H.-J. Eckoldt, J. Feldhaus, N. Golubeva, K. Honkavaara, M. Koerfer, T. Laarmann, A. Leuschner, L. Lilje, T. Limberg, D. Noelle, F. Obier, A. Petrov, E. Ploenjes, K. Rehlich, H. Schlarb, B. Schmidt, M. Schmitz, S. Schreiber, H. Schulte-Schrepping, J. Spengler, M. Staack, F. Tavella, K. Tiedtke, M. Tischer, R. Treusch, M. Vogt, A. Willner, J. Bahrdt, R. Follath, M. Gensch, K. Holldack, A. Meseck, R. Mitzner, M. Drescher, V. Miltchev, J. Rönsch-Schulenburg, and J. Rossbach, "Flash II: Perspectives and challenges," Nuclear Instruments and Methods in Physics Research Section A: Accelerators, Spectrometers, Detectors and Associated Equipment **635**, S2–S5 (2011).

19.   F. Tavella, A. Willner, J. Rothhardt, S. Hädrich, E. Seise, S. Düsterer, T. Tschentscher, H. Schlarb, J. Feldhaus, J. Limpert, A. Tünnermann, and J. Rossbach, "Fiber-amplifier pumped high average power few-cycle pulse noncollinear OPCPA," Opt Express **18**, 4689–4694 (2010).

20.   M. Schulz, R. Riedel, A. Willner, S. Düsterer, M. J. Prandolini, J. Feldhaus, B. Faatz, J. Rossbach, M. Drescher, and F. Tavella, "Pulsed operation of a high average power Yb:YAG thin-disk multipass amplifier," Opt. Express **20**, 5038–5043 (2012).

21.   F. Röser, T. Eidam, J. Rothhardt, O. Schmidt, D. N. Schimpf, J. Limpert, and A. Tünnermann, "Millijoule pulse energy high repetition rate femtosecond fiber chirped-pulse amplification system," Opt. Lett. **32**, 3495–3497 (2007).

22.   A. Willner, A. Hage, R. Riedel, I. Grguraš, A. Simoncig, M. Schulz, T. Dzelzainis, H. Höppner, S. Huber, M. J. Prandolini, B. Dromey, M. Zepf, A. L. Cavalieri, and F. Tavella, "Coherent spectral enhancement of carrier-envelope-phase stable continua with dual-gas high harmonic generation," Opt. Lett., OL **37**, 3672–3674 (2012).

23.   R. W. Boyd, *Nonlinear Optics*, 3rd revised edition. (Academic Press, 2008).

24.   P. M. Paul, E. S. Toma, P. Breger, G. Mullot, F. Augé, P. Balcou, H. G. Muller, and P. Agostini, "Observation of a Train of Attosecond Pulses from High Harmonic Generation," Science **292**, 1689–1692 (2001).

25.   P. Salières and M. Lewenstein, "Generation of ultrashort coherent XUV pulses by harmonic conversion of intense laser pulses in gases: towards attosecond pulses," Measurement Science and Technology **12**, 1818–1827 (2001).

26.   L. Keldysh, "Ionization in the field of a strong electromagnetic wave," Soviet Physics JETP **20**, 1307–1314 (1965).

27.   A. Perelomov, V. Popov, and M. Terentev, "Ionization of atoms in an alternating electric field," Soviet Physics JETP **23**, 924 (1966).

28.   M. Ammosov, N. Delone, and V. Krainov, "Tunnel ionization of complex atoms and of atomic ions in an alternating electromagnetic field," Soviet Physics - JETP **64**, 1191–1194 (1986).

29.   M. Bellini, C. Corsi, and M. C. Gambino, "Neutral depletion and beam defocusing in harmonic generation from strongly ionized media," Phys. Rev. A **64**, 023411 (2001).

30.   Y. Mairesse, "High-harmonics chirp and optimization of attosecond pulse trains," Laser Physics **15**, 863–87 (2005).

31.   F. Krausz and M. Ivanov, "Attosecond physics," Rev. Mod. Phys. **81**, 163–234 (2009).

32.   A. Rundquist, C. G. Durfee, Z. Chang, C. Herne, S. Backus, M. M. Murnane, and H. C. Kapteyn, "Phase-Matched Generation of Coherent Soft X-rays," Science **280**, 1412–1415 (1998).

33.   R. Paschotta, *Encyclopedia of Laser Physics and Technology*, 1. Auflage (Wiley-VCH Verlag GmbH & Co. KGaA, 2008).

34.   E. Constant, D. Garzella, P. Breger, E. Mével, C. Dorrer, C. Le Blanc, F. Salin, and P. Agostini, "Optimizing High Harmonic Generation in Absorbing Gases: Model and Experiment," Phys. Rev. Lett. **82**, 1668–1671 (1999).

35.   A. Paul, E. A. Gibson, X. Zhang, A. Lytle, T. Popmintchev, X. Zhou, M. M. Murnane, I. P. Christov, and H. C. Kapteyn, "Phase-matching techniques for coherent soft X-ray generation," IEEE Journal of Quantum Electronics **42**, 14 – 26 (2006).

36.   C. P. Hauri, W. Kornelis, F. W. Helbing, A. Heinrich, A. Couairon, A. My-syrowicz, J. Biegert, and U. Keller, "Generation of intense, carrier-envelope phase-locked few-cycle laser pulses through filamentation," Applied Physics B: Lasers and Optics **79**, 673–677 (2004).

37.   C.-J. Lai and F. X. Kärtner, "The influence of plasma defocusing in high harmonic generation," Opt. Express **19**, 22377–22387 (2011).

38.   A. Willner, F. Tavella, M. Yeung, T. Dzelzainis, C. Kamperidis, M. Ba-karezos, D. Adams, M. Schulz, R. Riedel, M. C. Hoffmann, W. Hu, J. Rossbach, M. Drescher, N. A. Papadogiannis, M. Tatarakis, B. Dromey, and M. Zepf, "Co-herent Control of High Harmonic Generation via Dual-Gas Multijet Arrays," Phys. Rev. Lett. **107**, 175002 (2011).

39.   G. D. Goodno, S. J. McNaught, J. E. Rothenberg, T. S. McComb, P. A. Thielen, M. G. Wickham, and M. E. Weber, "Active phase and polarization lock-ing of a 1.4 kW fiber amplifier," Opt. Lett. **35**, 1542–1544 (2010).

40.   D. Strickland and G. Mourou, "Compression of amplified chirped opti-cal pulses," Optics Communications **55**, 447–449 (1985).

41.   J. Limpert, N. Deguil-Robin, I. Manek-Hönninger, F. Salin, F. Röser, A. Liem, T. Schreiber, S. Nolte, H. Zellmer, A. Tünnermann, J. Broeng, A. Peters-son, and C. Jakobsen, "High-power rod-type photonic crystal fiber laser," Opt. Express **13**, 1055–1058 (2005).

42.   S. Hädrich, M. Krebs, J. Rothhardt, H. Carstens, S. Demmler, J. Limpert, and A. Tünnermann, "Generation of µW level plateau harmonics at high repeti-tion rate," Opt Express **19**, 19374–19383 (2011).

43.   S. Hädrich, H. Carstens, J. Rothhardt, J. Limpert, and A. Tünnermann, "Multi-gigawatt ultrashort pulses at high repetition rate and average power from two-stage nonlinear compression," Opt Express **19**, 7546–7552 (2011).

44.   S. Hädrich, S. Demmler, J. Rothhardt, C. Jocher, J. Limpert, and A. Tün-nermann, "High-repetition-rate sub-5-fs pulses with 12 GW peak power from fiber-amplifier-pumped optical parametric chirped-pulse amplification," Opt. Lett. **36**, 313–315 (2011).

45.   A. Paul, R. A. Bartels, R. Tobey, H. Green, S. Weiman, I. P. Christov, M. M. Murnane, H. C. Kapteyn, and S. Backus, "Quasi-phase-matched generation of coherent extreme-ultraviolet light," Nature **421**, 51–54 (2003).

46.   E. M. Bothschafter, A. Schiffrin, V. S. Yakovlev, A. M. Azzeer, F. Krausz, R. Ernstorfer, and R. Kienberger, "Collinear generation of ultrashort UV and XUV pulses," Optics Express **18**, 9173 (2010).

47.   J. P. Farrell, B. K. McFarland, P. H. Bucksbaum, and M. Gühr, "Calibration of a high harmonic spectrometer by laser induced plasma emission," Opt. Express **17**, 15134–15144 (2009).

48.   C. Altucci, T. Starczewski, E. Mevel, C.-G. Wahlström, B. Carré, and A. L'Huillier, "Influence of atomic density in high-order harmonic generation," J. Opt. Soc. Am. B **13**, 148–156 (1996).

49.   I. Vullkaj, A. Done, and M. Xhoxhi, "The Characterization of a Xenon Gas Jet into Vacuum by Means of Interferometric Technique," AIP Conference Proceedings **1203**, 612–617 (2010).

50.   B. Landgraf, M. Schnell, A. Sävert, M. C. Kaluza, and C. Spielmann, "High resolution 3D gas-jet characterization," Review of Scientific Instruments **82**, 083106–083106–6 (2011).

51.   T. Ditmire and R. A. Smith, "Short-pulse laser interferometric measurement of absolute gas densities from a cooled gas jet," Opt. Lett. **23**, 618–620 (1998).

52.   M.-C. Chen, M. R. Gerrity, S. Backus, T. Popmintchev, X. Zhou, P. Arpin, X. Zhang, H. C. Kapteyn, and M. M. Murnane, "Spatially coherent, phase matched, high-order harmonic EUV beams at 50 kHz," Opt. Express **17**, 17376–17383 (2009).

53.   X. Wang, M. Chini, Q. Zhang, K. Zhao, Y. Wu, D. A. Telnov, S.-I. Chu, and Z. Chang, "Mechanism of quasi-phase-matching in a dual-gas multijet array," Phys. Rev. A **86**, 021802 (2012).

54.   A.-T. Le, R. D. Picca, P. D. Fainstein, D. A. Telnov, M. Lein, and C. D. Lin, "Theory of high-order harmonic generation from molecules by intense laser pulses," Journal of Physics B: Atomic, Molecular and Optical Physics **41**, 081002 (2008).

Acknowledgment

Selbständigkeitserklärung

Hiermit versichere ich, dass ich diese Arbeit selbständig verfasst und keine anderen als die angegebenen Quellen und Hilfsmittel Benutzt habe. Außerdem versichere ich, dass ich die allgemeinen Prinzipien wissenschaftlicher Arbeit und Veröffentlichung, wie sie in den Leitlinien guter wissenschaftlicher Praxis der Carl von Ossietzky Universität Oldenburg und Hochschule Emden/Leer festgelegt sind, befolgt habe.